Journal of Pharmacognosy and Phytochemistry
Available online at www.phytojournal.com

E-ISSN: 2278-4136
P-ISSN: 2349-8234
Impact Factor (RJIF): 6.35
www.phytojournal.com
JPP 2025; 14(5): 348-368
Received: 15-06-2025
Accepted: 19-07-2025

All authors names and affiliations are given below, after the references.

Phytochemical analysis and bioactivities of *Rhizophora mucronata Lam.* from Djibouti: *in vitro* and *in silico* approaches

Ahmed Said Mohamed, Abdirahman Elmi, Fatouma Mohamed Abdoul-Latif, Rosella Spina, Imane Yamari, Maha AY Kordofani, Ali Mérito, Arnaud Risler, Dominique Laurain-Mattar and Samir Chtita

DOI: https://doi.org/10.22271/phyto.2025.v14.i5e.15592

Abstract
This study investigates the phytochemical composition and biological activities of crude extracts from *Rhizophora mucronata Lam.* collected in the Republic of Djibouti. Ethanolic extracts from leaves, stems, and flowers were analyzed, revealing high yields extractsusing 90% ethanol extraction. Flavonoid quantification showed the highest content in leaves (0.144 µg QE/mg extract), followed by flowers (0.059 µg QE/mg), and stems (0.041 µg QE/mg). HPLC-MS/MS analysis identified six major phytochemicals, including utin (C1), kaempferol derivatives (C2), flavone (C3), quinic acid (C4), 3-(benzoyloxy)-2-hydroxypropyl alpha-D-glucopyranosiduronic acid (C5), and naringin (C6). The flower extract exhibited the strongest antibacterial effect, particularly against *Staphylococcus aureus* (MIC = 640 µg/mL), whereas leave and stem extracts showed weaker activity (MIC > 2560 µg/mL for most Gram-negative bacteria). Antioxidant potential was evaluated using DPPH and ABTS assays, with flower extracts demonstrating the highest radical-scavenging activity (IC_{50} = 159 µg/mL for DPPH and 137.5 µg/mL for ABTS). Furthermore, Molecular docking studies revealed strong binding interactions between naringin and key *S. aureus* proteins (binding energy -10.2 kcal/mol for 2W9G) and with the antioxidant enzyme catalase (2CAG, -11.1 kcal/mol), supporting its potential pharmacological relevance. ADMET analysis showed good solubility for all compounds, with C3 and C4 exhibiting the best bioavailability. Naringin displayed moderate toxicity (LD_{50} = 2300 mg/kg). These findings suggest that *Rhizophora mucronata* extracts, particularly from flowers, could serve as promising natural sources of antibacterial and antioxidant agents.

Keywords: *Rhizophora mucronata*, antibacterial, antioxidant, Docking and dynamic molecular and ADMET

Introduction
Rhizophora is a genus known for its effective medicinal effects. The leaves and roots are the plant parts used to treat ulcers (Krishnamoorthy *et al.*, 2011) [25], diarrhea, fever, and burns. Traditional use of bark and leaf extracts have been found to be good agents with antibacterial, antiulcerogenic, and anti-inflammatory properties (Kaur *et al.*, 2018) [22].
Mangrove covers most of the coastal part of the Republic of Djibouti. There are particularly 4 plants of the Mangrove kingdom: *Avicennia marina* (Mohamed *et al.*, 2023) [31], *Ceriops tagal*, *Bruguiera gymnorrhiza*, and *Rhizophora mucronata*, which will be the subject of this study.
Rhizophora mucronata is a species of flowering plant in the family *Rhizophoraceae.* (Schwarzbach & Ricklefs, 2000) [45], characterized by its curly roots, also known as red mangrove (Warui *et al.*, 2020). It is a mangrove native to tropical and subtropical coastal areas (Rohini & Das, 2009) [42], extending from the east coast of Africa to Asia and Australia and the islands of the eastern Pacific Ocean.
Specifically, the *Rhizophora mucronata* possesses a phytochemical composition that supports multiple biological activities. Its antidiarrheal efficacy is widely recognized in ethnomedicine (Camilleri & Murray, 2022) [6], and the plant has been traditionally used to treat symptoms such as diarrhea, constipation, nausea, and diabetes (Nabeelah Bibi *et al.*, 2019) [35]. Various plant parts including the bark, roots, leaves, fruits, and flowers have demonstrated therapeutic potential for inflammation, wounds, ulcers, diabetes, and microbial infections (Bandaranayake, 1998; Duke, 1992) [4, 11]. The technicality of extraction and the part of the plant are also

Corresponding Author:
Ahmed Said Mohamed
Centre d'Étude et de Recherche de Djibouti, Institut de Recherche Médicinale, Route de l'aéroport, Djibouti

influential parameters of biological activity as for example, the decoction of the root is used to treat diabetes and hypertension, while the infusion of the leaves is used to treat fever. Kishen *et al*. (2021) [24] studied the potential of plant leaf in the presence of *Streptomyces* species (Streptomyces species are the largest genus of Actinobacteria, gram-positive and are found in soil, decaying vegetation and mangrove leaves.) against breast cancer (Kishen *et al*., 2021) [24].

In 2023, a study was conducted by Asbin *et al*. showing the toxicity and anticancer potential by *in vivo* testing of methanolic extracts of *Rhizophora mucronata* leaf obtained by the soxhlet method, against breast cancer. Based on this work, it was concluded that the methanolic extract of *Rhizophora mucronata* leaves was safe at both higher and lower doses

(1000 and 100 mg/kg) and could be evaluated for pharmacological study (Mary X *et al.*, 2023) [31].

Rhizophora mucronata has been shown to have the potential to act as a source of useful drugs due to their antibacterial activity against Streptococcus *agalactia*e and Aeromonas *hydrophila* in particular (Vittaya *et al*., 2022a) [49]. Determination of biologically active compounds, such as the predominant contents of saponin, phenolic compounds and flavonoids in the extracts, provided evidence for the presence of antimicrobial phytochemical components. Such species could provide natural bioactive agents to replace synthetic compounds that are curr ently used to treat diseases caused by aquatic pathogens (Vittaya *et al*., 2022a) [49].

Djibouti, an East African country characterized by a tropical, hot, and humid climate, provides a unique environment for studying the phytochemical properties of *Rhizophora mucronata* under extreme climatic conditions. It also focuses on the evaluation of the potential of antioxidant and antibacterial activities.

2. Material and Methods

2.1. Plant samples and botanical characterization.

2.1.1. Plant collection area.

The *Rhizophora mucronata* was harvested in Godoria, a mangrove swamp area south of the Red Sea located in the Obock district in the northeast of Djibouti in June 2020, the localization coordinate of the college N12° 09’ 13”, E43° 24 30”; a total mass of 10 kg before dehydration. The studies were carried out on the different parts of the plant (leaf, stem, and flower) (Figure 1).

Fig 1: Godoria: Collection site in the northeast of Djibouti.

2.1.2. Morphological characteristics.

Rhizophora mucronata Lam. is an evergreen tree, small to medium in size, growing to a height of about 20 to 25 meters on the banks of rivers. Stem up to 40 cm in diameter, straight, with distinctive aerial roots and dark black bark, horizontally fissured. Leaves compact, simple, oppositely arranged, broadly elliptic to oblong-elliptic, leathery, glossy, dark green to yellowish green, usually about 12 cm long and 6 cm wide; margins smooth with pointed apex and distinctive hair-like tip of up to 5 mm long; tapering at both ends. Creamy white flowers, arranged in axillary heads, leathery with short thick stalks; calyx persistent. The fruit is elongated ovoid berry, single seeded, up to 7 cm long. The seeds are viviparous and start to develop whilst still attached to the tree.

2.2. Experimental reagents.

The study utilized various organic solvents and analytical reagents, including DPPH (1,1-diphenyl-2-picrylhydrazyl), ABTS (2,2′-azino-bis(3-ethylbenzothiazoline-6-sulfonic acid)), ascorbic acid, $FeCl_3$ (iron(III) chloride), Folin-Ciocalteu reagent, quercetin, hydrochloric acid, and H_2SO_4 (sulfuric acid), all of which were sourced from Sigma-Aldrich and Acros Organics.

2.3. Plant extracts.

The extraction process was adapted from the protocol reported by (Mohamed *et al*., 2023) [31]. A quantity of 10 g of powdered material from the leaves, stems, and flowers of *Rhizophora mucronata* was individually macerated in 100 mL of ethanol at varying concentrations (90%, 70%, and 50%) for 24 hours at ambient temperature. The mixtures were filtered through a coffee filter, and the filtrates were subsequently centrifuged at 4000 rpm for 15 minutes at room temperature. The supernatants were then concentrated using a rotary evaporator. The resulting crude extracts were stored at approximately 4 °C. R(%) = 100 m_{ext}/m_{samp}. Where R

represents the percentage yield, m_{ext} is the mass of the obtained extract after solvent evaporation (mg), and m_{samp} denotes the mass of the initial dry plant material (mg) *(Falleh et al.,* 2008) [13].

2.4. Determination of total flavonoid content (TFC).

The total flavonoid content was determined using the same protocol reported by Mohamed *et al.*, 2023 [31]. Quercetin was used as a reference standard, and the total flavonoid content was expressed as milligrams of quercetin equivalents (mg QE/100g dry matter).

2.5. Evaluation of antibacterial and antioxidant activities.

2.5.1. Antibacterial activity.

The antibacterial activities of the leaf, stem, and flowers crude extracts of *R. mucronata* were tested against the Gram-positive strain *Staphylococcus aureus ATCC 29213* and *Enterococcus faecalis CIP 103214*, and the Gram-negative strains *Pseudomonas aeruginosa ATCC 27853*, *Klebsiella pneumoniae CIP 110855*, *Escherichia coli ATCC 25922*, *Acinetobacter baumannii* (non-resistant clinical strain), and *Enterobacter cloacae* (non-resistant clinical strain). The samples tested were prepared separately: at 51.2 mg/mL in DMSO for leaves and stems and at 25.6 mg/mL of DMSO. To ensure dissolution and homogenization, the samples were sonicated for 1 hour in an ultrasonic bath, and incubated overnight at 35°C. The DMSO samples were then prediluted by 1/5 in water; this diluted solution is used for the tests in order to have a maximum of 5% DMSO in the final wells. Antibacterial activities were carried out on the PhotoNS Platform of the L2CM Laboratory, Université de Lorraine.

MIC was evaluated by microdilution method in MHB-CA medium on a final volume of 100 µL (50 µL of sample dilution + 50 µL of bacterial inoculum) (Elmi *et al*., 2020) [12]. The controls performed on each plate are: medium control only, medium + sample control and bacteria control (growth control). A range of successive dilutions of 1/2 was tested for each sample. For stem and leaves: range from 2560 to 10 µg/mL for flowers: range from 1280 to 5 µg/mL.

2.5.2. Antioxidant activity.

2.5.2.1. DPPH radical-scavenging activity.

The free-radical-scavenging activity of the *Rhizophora mucronata* extracts were measured using an improved DPPH assay same protocol by Mohamed *et al.* (2023) [31]. The protocol is detailed in the information support.

2.5.2.2. ABTS radical-scavenging activity.

The ability of the extract to scavenge ABTS radical was determined according to a previously published method (See in Supporting Information) (Mohamed *et al.*, 2023) [31].

2.6. HPLC-MS/MS analysis of extracts.

The HPLC/MS system was configured with a quaternary solvent delivery pump, a Grace-Discovery Alltima C18 (150 mm × 4.6 mm, 5 µm) reversed-phase column and a linear ion trap mass spectrometer (LTQ-MS, Thermo Electron Corporation, Waltham, MA, USA), coupled to an Orbitrap high-resolution mass spectrometer (HRMS, Thermo Electron Corporation, Waltham, MA, USA). The LTQ-Orbitrap featured an electrospray ionization (ESI) interface, operating in both polarity (positive/negative) ion modes. The mobile phase is a mixture of water with 0.1% formic acid (Solvent A) and methanol with0.1 % formic acid (Solvent B). The elution program is a linear gradient 10% to 95% B from 0 min to 25 min then returned at 10% B for 5 min. Injection speed was constant at 0.2 mL/ min.

Electrospray ions were generated using a capillary voltage of 3.5 kV and 2.5 kV for positive and negative mode respectively. The vaporizer temperature was 320 and the scan interval m/z ranged 120-1200 in MS and MS/MS. For the structural identification we relied on two databases and ions fragmentations analysis. The first database is a local database containing 90 phenolic compounds and 10 alkaloids. This database was built using MzVault software (Thermo Scientific). Also, we used for an identification online open database Metlin (accessed 9 and 10 September 2024).

2.7. Computational investigation of bioactive compounds.

2.7.1. Evalution of Anti-Staphylococcus aureus activity.

The crystal structures of dihydrofolate reductase (PDB ID: 2W9G) (Heaslet *et al*., 2009) [16], clumping factor A (PDB ID: 1N67) (Deivanayagam *et al*., 2002) [10], and structure of penicillin G acyl-Penicillin binding protein 2a from methicillin resistant Staphylococcus aureus strain 27r at 2.45 Å resolution (PDB ID: 1MWT chain B) (Lim & Strynadka, 2002) [27] were retrieved from the RCSB Protein Data Bank available online at (www.RCSB.org). To prepare these structures for molecular docking analysis, the existing ligands and water molecules were eliminated using Discovery Studio 2024 software. Additionally, polar hydrogen atoms and Kollman charges were added to the proteins using PyRx software. To facilitate the docking process, grid boxes were positioned to cover all the proteins. Docking scores, measured in kcal/mol, were obtained for each compound identified in flower extract, and these scores were utilized to rank the compounds based on their binding affinity. Subsequently, the molecular interactions between the proteins and the selected ligands were visualized using Discovery Studio Visualizer 2024 (Nguyen *et al.*, 2024) [38].

2.7.2. Antioxidant evaluation by *in silico*

Molecular docking studies were performed using PyRx software (Mohamed *et al*., 2023; Hashem *et al*., 2024; Yousaf *et al*., 2024) [31, 15, 52] to evaluate the affinity of six abundant phytochemical constituents of *Rhizophora mucronata* toward Catalase compound II (2CAG), which is an enzyme catalyzing redox reaction. All details for protein preparation are described in the supporting information.

2.7.3 Molecular dynamics simulations

To investigate the dynamic behavior of ligand-protein interactions under physiologically relevant conditions, Molecular Dynamics (MD) simulations were conducted to model the movement of water, ions, and macromolecules. These simulations were essential for capturing the structural fluctuations of protein-ligand complexes in response to factors such as temperature and solvent conditions (Nejjari *et al*., 2024; Toughzaoui *et al*., 2025) [37, 45]. The simulations were performed for 100 ns using the Desmond module of the Schrödinger Suite. The initial protein-ligand complexes were obtained from docking studies, which provided a static view of ligand binding. Unlike docking, which offers a snapshot of the ligand's binding pose, MD simulations allow for the examination of atomic motions over time by numerically integrating Newton's equations of motion (Hernández-Rodríguez *et al*., 2016) [18]. These simulations provide insights into ligand binding and `the stability of the complex in a dynamic environment. Before the simulation, the protein-ligand complexes were preprocessed with the Protein

Preparation Wizard in Maestro, involving extensive optimization and minimization (*Schrödinger Release 2018-4. Protein Preparation Wizard; Epik; Schrödinger, LLC: New York, NY, 2018*, n.d.). System preparation was performed using the System Builder tool, and the OPLS3e force field was applied during the simulation (Roos *et al*., 2019) [43]. Solvent molecules were modeled with the TIP3P model in an orthorhombic box (Mark & Nilsson, 2001) [30], and counterions were added to neutralize the system. A physiological salt concentration of 0.15 M NaCl was included to replicate natural conditions. Equilibration of the system was carried out in two stages: an NVT ensemble for 1 ns, followed by an NPT ensemble for 10 ns to stabilize temperature and pressure. After equilibration, production simulations were performed for 100 ns. The system was maintained at 300 K and 1 atm using the Martyna-Tuckerman-Klein barostat. Trajectories were saved every 100 ps, and the stability of the system was assessed by calculating the root mean square deviation (RMSD) of the protein-ligand complex. Subsequent analyses focused on the root mean square fluctuation (RMSF) of protein residues and protein-ligand interactions.

2.7.4. ADMET analysis

ADMET (Absorption, Distribution, Metabolism, Elimination, Toxicity) analysis were calculated using the Swiss ADME (Ioakimidis *et al*., 2008) [21] for assessing the drug ability and to filter the ligand molecules at an early stage of identifying the new inhibitors. Toxicity was the degree to which a substance can damage an organism or substructure of the organism. The predictions of toxicity of the compounds were essential to reduce the cost and labor of a drug's preclinical and clinical trials. The toxicity evaluation was performed also using the ProTox platform (Banerjee *et al*., 2018) [5]. It gave predicted toxicity values, Hepatotoxicity, Neurotoxicity, Respiration toxicity, cardiotoxicity, cytotoxicity, mutagenicity, and LD50 values of selected compounds.

3. Results and discussions.

3.1 Maceration extraction yield.

In this present study, we used hydroethanol as an extraction solvent using mild conditions to avoid evaporation and/or degradation of volatile organic products. The choice of the extractor is made between three hydroethanol by varying the volume proportion ethanol:water namely ethanol 90%; ethanol 70% and ethanol 50%. The results were presented in Figure 2. Ethanol at 90% provided the highest extractive yield across all three plant parts compared to 70% and 50% ethanol. Specifically, using 90% ethanol resulted in extract yields of 68% for leaves, 45% for stems, and 54% for flowers. These results suggest that the extractive yield is positively correlated with the alcohol-to-water ratio: the higher the ethanol concentration, the greater the yield. Therefore, for the remainder of this study, we focused our analyses on the extracts obtained with 90% ethanol, which demonstrated the best yields.

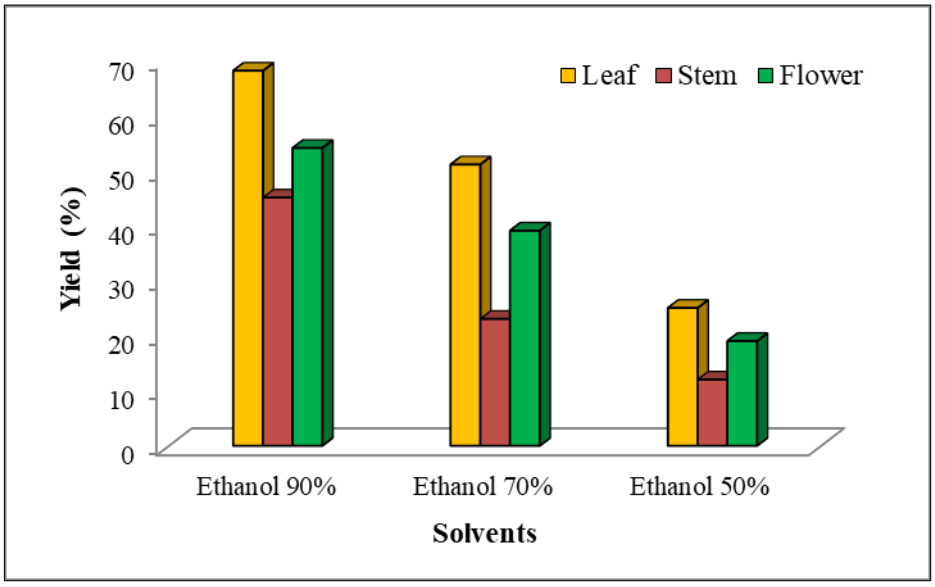

Fig 2: Comparative diagrams of extraction yield by maceration of different parts of *Rhizophora mucronata.*

3.2. Quantification of total flavonoids (TFC).

The TFC of different parts of *Rhizophora mucronata* were presented in Table 1. The variation in flavonoid content among different plant parts is relatively minor and does not exhibit strong statistical significance. A marked disparity in flavonoid richness is observed among the different plant parts. Total flavonoid content (TFC) ranges from 0.144 to 0.041 µg QE/mg of dry extract. The crude leaf extract exhibits the highest TFC at 0.144 µg QE/mg, whereas the flower and stem extracts show significantly lower levels, with 0.059 and 0.041 µg QE/mg respectively, corresponding to reductions of approximately 2.4- to 3.5-fold.

Table 1: Results obtained from TFC of crude ethanolic extracts expressed in µg QE/100g DM and µg QE/mg dry extract respectively.

Samples	(µg QE/100 g DM)	µg QE/mg dry extract
Leaf	9.77±1.6	0.144±0.01
Stem	1.86±0.1	0.041±0.001
Flower	3.20±0.6	0.059±0.001

3.3. Biological activities

3.3.1. Antibacterial activity *in vitro* analysis.

Rhizophora mucronata has garnered attention for its antibacterial properties, particularly against various

pathogenic bacteria. Numerous studies have demonstrated the efficacy of different extracts from *Rhizophora mucronata* in inhibiting bacterial growth, which is attributed to the presence of various bioactive compounds (Nur *et al*., 2022) [39].

In this study, both leaf and stem extracts show weaker antibacterial activity, with MIC values mostly above 2560 µg/mL against most bacteria, particularly for the gram-negative strains (e.g., *P. aeruginosa*, *E. coli*, *K. pneumoniae*), which are generally more resistant to plant-derived compounds. The flower extract shows the most potent activity, with lower MIC values compared to the leaf and stem extracts, especially against *S. aureus* (640 µg/mL) and *A. baumannii* (640 µg/mL). The MIC against *S. aureus* and *E. faecalis* show relatively lower values, suggesting that the extracts are more effective against gram-positive bacteria. In particular, the flower extract exhibits the best inhibitory effect against *S. aureus* with an MIC of 640 µg/mL, while both leaf and stem extracts exhibit higher MIC values (1280 µg/mL). The targeted action of extracts from this plant against *S. aureus* has also been reported in the literature (Fareza *et al*., 2018; Nur *et al*., 2022; Vittaya *et al.*, 2022b) [14, 39, 49].

Table 2: Minimum Inhibitory Concentrations (MIC) of leaf, stem, and flower extracts against various pathogenic bacteria. Values are expressed in µg/mL.

Bacteria	MIC (µg/mL)		
	Leaf extract	Stem extract	Flower extract
S. aureus	1280	1280	640
E. faecalis	>320	>320	>160
P. aeruginosa	>2560	>2560	>1280
E. coli	>2560	>2560	>1280
K. pneumoniae	>2560	>2560	>1280
A. baumannii	>2560	>2560	>640
E. cloacae	>2560	>2560	>1280
C. glabrata	>512	>512	>512

3.3.2. Antioxidant activity analysis.

3.3.2.1. DPPH method.

DPPH radical cation scavenging activity of leaf, stem, and flower extracts of *Rhizophora mucronata* were given in Table S2 in supplementary information and Figure 3. The results obtained clearly show that the ethanolic extracts of *Rhizophora mucronata* have an antioxidant effect which varies according to the part of the plant considered (Al-Mur, 2021; H. A. H. Ibrahim *et al*., 2021) [2, 19]. However, this antioxidant power is visibly proportional to the concentration of dry extract.

The crude ethanolic flower extract presented the best antioxidant activity with IC_{50}= 159 µg/mL compared to the other crude leaf and stem extracts. The crude leaf and stem extracts have an interesting antioxidant effect (IC_{50} = 258 and 264 µg/mL respectively), obviously less important than the crude flower extract. The antioxidant activity profiles of the leaf and stem extracts were around 1.64 less significant (258 *vs.* 264 µg/mL) than the result of the crude flower extract. A study was carried out in 2016 on the evolution of the antioxidant activity of the same plant *Rhizophora mucronata* from Indian sundarban mangrove, showing that the ethanolic extract of the leaf gave an interesting inhibition value of 6.65 µg/mL (Adhikari *et al*., 2016) [1].

Antonius *et al*. in 2021 also performed the ethanolic maceration of *Rhizophora mucronata* leaf with a slightly different procedure than ours. The result obtained showed a very interesting antioxidant effect with an IC_{50} value equal to 20.99 µg/mL compared to the reference (Vitamin C) IC_{50} 9.62 µg/mL. This value is 7 times more interesting than our result obtained from the ethanolic extract of flower (158 µg/mL) (Rumengan *et al*., 2021) [44].

In 2023, a study was conducted by Usman *et al*. regarding the evaluation of the antioxidant activity of the methanolic extract of *Rhizophora mucronata* leaf. The methanolic extract gave an IC_{50} value by the DPPH method 0.101 mg/mL (101 µg/mL) compared to vitamin C (IC_{50} = 0.005 µg/mL). This result is 1.6 times better than the result obtained from the IC_{50} of the Djiboutian *Rhizophora mucronata* flower extract. It can be deduced that the localization of the plant (environment and climate) plays a primordial role in the phytochemical composition by influencing the effectiveness of its antioxidant activity.

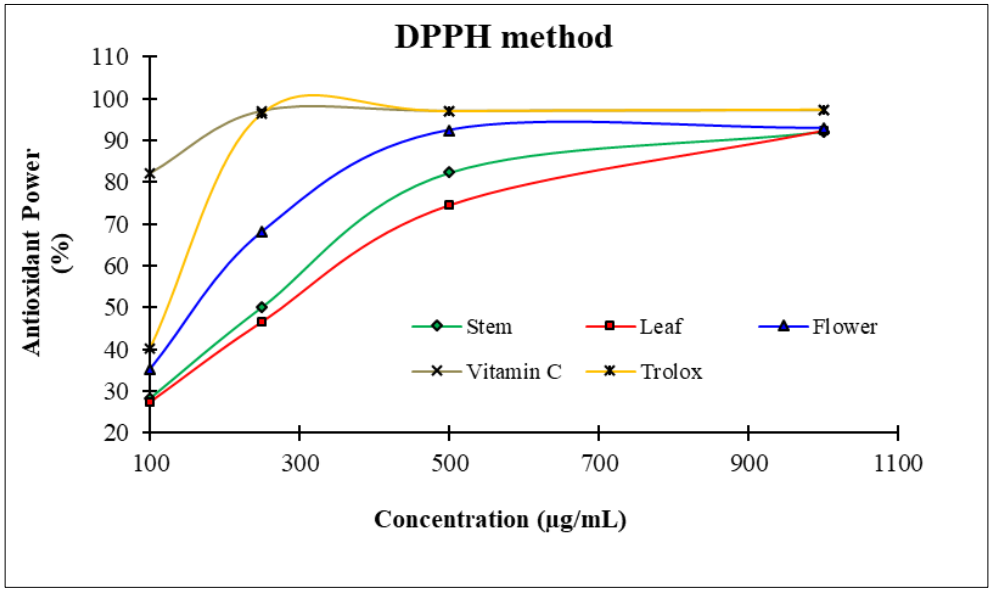

Fig 3: Antioxidant activity using DPPH method at different concentrations of the crude ethanolic extracts (Leaf, Stem, and Flower) in µg/mL.

3.3.2.2. ABTS method.

The ethanolic flower extract has also the best antioxidant activity with ABTS method with IC_{50} value of 137.5 µg/mL. This latter is followed by the stem and leaf extracts with IC_{50} values 162.5 µg/mL and 225 µg/mL respectively (Figure 4 and Table S3 in Supporting Information). Crude stem and leaf extracts have widely different antioxidant activity IC_{50} 162.5 *vs.* 225 µg/mL respectively.

Table 3: IC_{50} values (half-maximal inhibitory concentration) of antioxidant activity by DPPH and ABTS methods for the crude ethanolic extracts of different parts of *Rhizophora mucronata*.

	IC_{50} (µg/mL)	
Samples	**DPPH**	**ABTS**
Leaf	264	225
Stem	258	162.5
Flower	159	137.5
Vitamin C*	<0.125	<0.125
Trolox*	0.14	<0.125

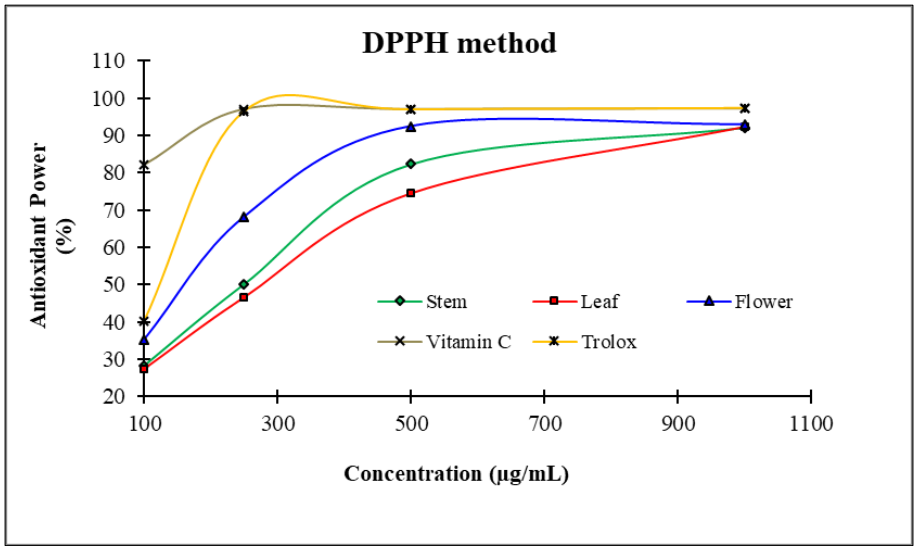

Fig 4: Antioxidant activity using ABTS method at different concentration of the crude ethanolic extracts (Leaf, Stem, and Flower) in µg/mL.

There are many studies illustrating the antioxidant potential of the *Rhizophora mucronata* plant (Chelliah *et al*., 2023; Rahmawati *et al*., 2023) [7, 41]. Sur *et al*., in 2015, showed an antioxidant efficacy of the hydromethanolic extract (20:80) of the leaf with an IC_{50} value of 1.42 µg/mg by the ABTS method and IC_{50} = 42.93 µg/mg by the DPPH method.

Sully *et al*., in 2015 also evaluated the antioxidant activity of the parts of *Rhizophora mangle L.* namely the leaves, bark, and roots by the ABTS method. This study determined the IC_{50} value of each extract of *Rhizophora mucronata*: 260 µg/mL for the leaves, 320 µg/mL for the bark and finally 350 µg/mL for the roots. In terms of comparison, the IC_{50} value obtained for the leaf extract of *Rhizophora mucronata* Djiboutian is slightly lower (225 *vs.* 260 µg/mL) (Cruz *et al*., 2015) [8].

3.4. Phytochemical profile by HPLC-MS/MS analysis.

The three ethanolic crude extracts were analyzed using LC-MS/MS and their phytochemical profiles were evaluated (Figure 5). Significant peaks are observed at 17.94 min (in the leaf extract), 22.04 min (in the stem extract), and 22.09 min (in the flower extract). The identification of the compounds was based on the comparison of MS/MS spectra with our in-house database building in MzVault software, and online database such as Metlin.

In ethanolic extracts of *Rhizophora mucronata*, 6 flavonoid compounds were identified: Rutin (C1), kaempferol 3-O-α-rhamnopyranoside-7-O- β -glucopyranoside (C2), flavone (C3), quinic acid (C4), 3-(benzoyloxy)-2-hydroxypropyl α-D-glucopyranosiduronic (C5), and naringin (C6) (Table 4 and Figures 5 and 6).

Rutin (C1) was detected in all the plant parts studied in this work, with a retention time (RT) of 17.94 minutes. The $[M-H]^-$ peak at m/z 609 is characteristic of rutin, a flavonoid commonly found in plants. This identification was confirmed through comparison with a database of standards recorded under the same analytical conditions.

Kaempferol 3-O-α-rhamnopyranoside-7-O-β-glucopyranoside was exclusively found in the leaf extract (RT: 18.63 minutes). Its identification was based on fragment degradation patterns and supported by a previous study (L. F. Ibrahim *et al*., 2016). The molecular structure of this compound consists of kaempferol, a flavonoid, linked to two sugar units: rhamnose (α-rhamnopyranoside) and glucose (β-glucopyranoside). The fragment ion at m/z 447 suggests the loss of glucose (162 Da), while the fragment at m/z 285 indicates the stepwise loss of both glucose and rhamnose, a common fragmentation pattern for flavonoids in mass spectrometry.

Flavone ($C_{15}H_{10}O_2$), a basic flavonoid structure, was detected in both the leaf and stem extracts (RT: 22.06 minutes) and was identified through MzVault. Quinic acid ($C_7H_{12}O_6$), a known metabolite, was found in the stem and flower extracts (RT: 1.91 minutes) and identified using both MzVault and Meltin. A complex glucoside derivative, 3-(Benzoyloxy)-2-hydroxypropyl α-*D*-glucopyranosiduronic acid ($C_{16}H_{20}O_{10}$), was identified exclusively in the flower extract (RT: 15.49 minutes) with reference to our database.

Finally, naringin (C6), a flavanone, was detected exclusively in the flower extract (RT: 20.35 minutes). It was identified based on ion fragmentation patterns and confirmed by the literature (Xu *et al*., 2009) [51]. The peak at m/z 579.15 corresponds to the protonated molecular ion ($[M-H]^-$) of naringin. Fragment ions at m/z 271.05 and m/z 119.05 are characteristic of the flavonoid aglycone fragments, typically resulting from the cleavage of glycosidic bonds and subsequent stabilization of the flavonoid core structure (Figures S5 and S6, Supporting Information).

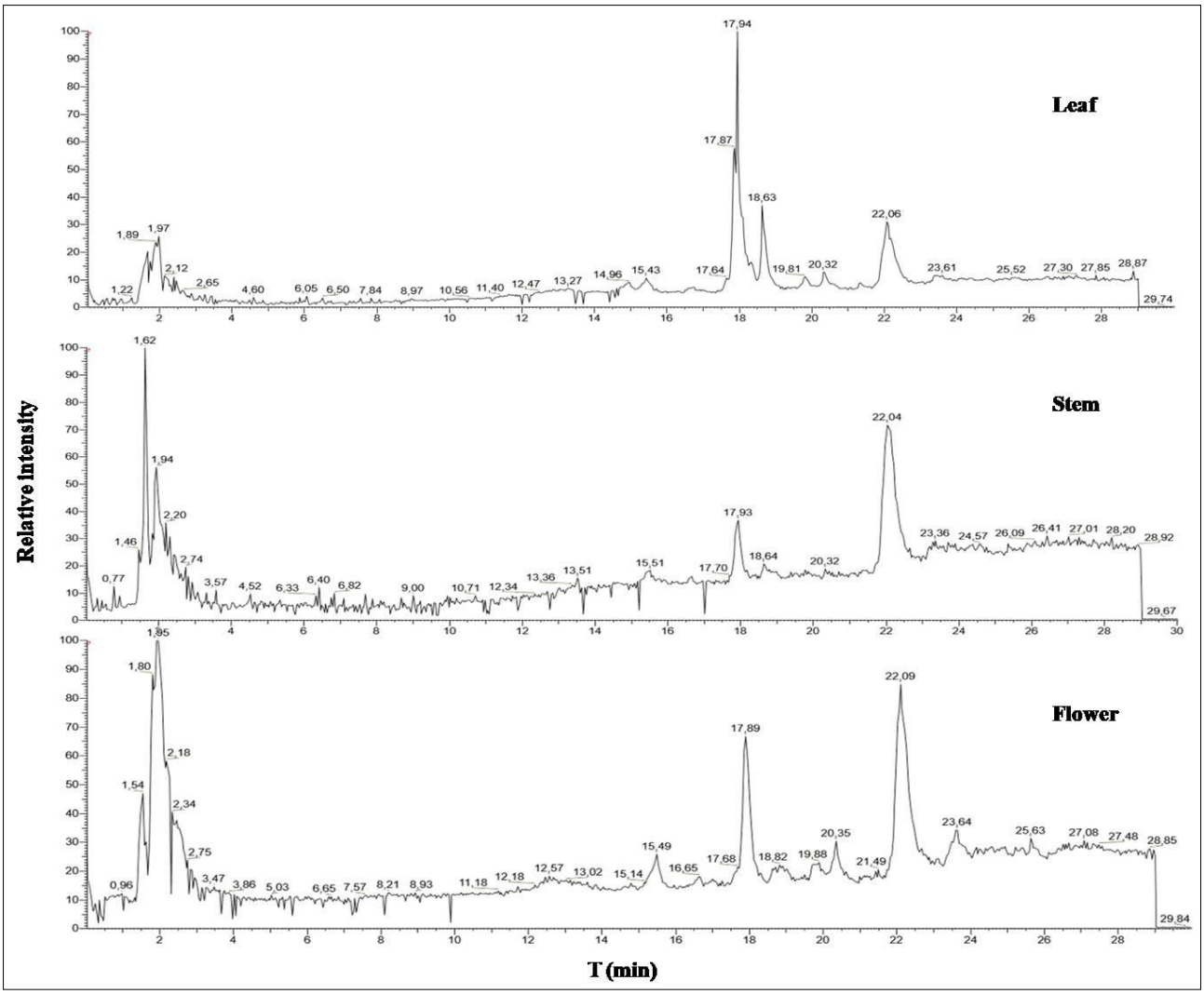

Fig 5: LC chromatogram analysis of the crude extracts in negative mode for different parts: (Leaf, Stem, and Flower extracts) of *Rhizophora mucronata*.

Table 4: Characteristic data from HR-LC-MS/MS analysis of six negative mode present in different parts of *Rhizophora mucronata.*

Id Compound	Molecules names	Retention time (min)	Formula	Theoretical m/z [M - H]$^-$	[M-H]$^-$ exp	Leaf extract	Stem Extract	Flower Extract	Identification
C1	Rutin	17.94	$C_{27}H_{30}O_{16}$	609.52	609.15	+	+	+	MzVault
C2	Kaempferol 3-O-α-rhamnopyranoside-7-O- β -glucopyranoside	18.63	$C_{27}H_{30}O_{15}$	593.15	593.15	+	-	-	Ion fragmentation
C3	Flavone	22.06	$C_{15}H_{10}O_2$	221.24	262.98	+	+	-	MzVault
C4	Quinic acid	1.91	$C_7H_{12}O_6$	191.17	191.06	-	+	+	MzVault
C5	3-(Benzoyloxy)-2-hydroxypropyl alpha-D-glucopyranosiduronic acid	15.49	$C_{16}H_{20}O_{10}$	371.32	371.10	-	-	+	MzVault
C6	Naringin	20.35	$C_{27}H_{32}O_{14}$	579.17	579.15	-	-	+	Ion fragmentation

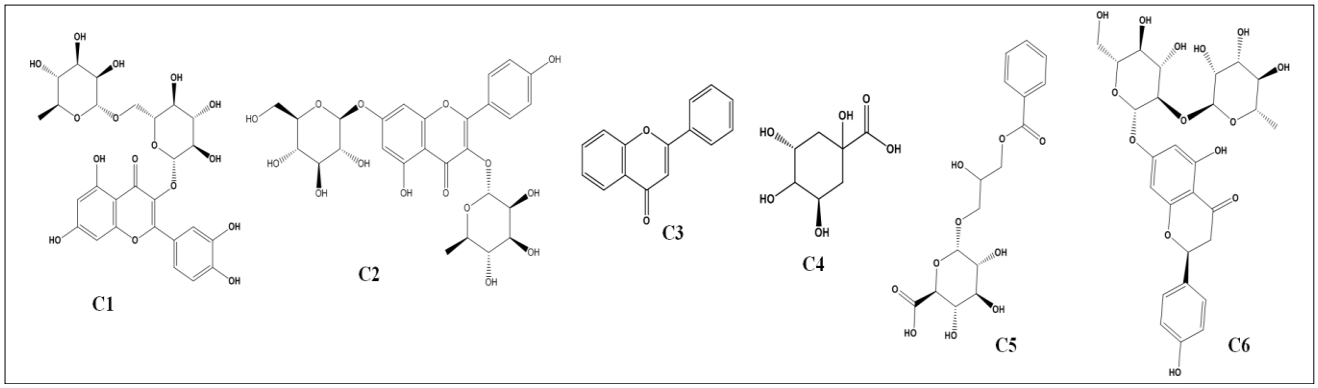

Fig 6: Semi-developed structure of six compounds identified HR-LCMS/MS.

3.5. Evaluation of antibacterial and antioxidant activities by *in silico*.

3.5.1. Molecular docking antibacterial screening.

The ethanolic extract of flowers showed the best biological response against the bacterium *S. aureus*. For that, we evaluated the compounds identified by LCMS from the flower extract against three proteins responsible for bacterial pathogenesis (2W9G, 1N67, and 1MWT chain B) by *in silico*. Rutin (C1), quinic acid (C4), 3-(benzoyloxy)-2-hydroxypropyl alpha-D-glucopyranosiduronic acid (C5), and naringin (C6) showed good affinities with the targeted proteins. Noteworthy observation, that naringin (C6) and rutin (C1) gave the best free binding energies for the three protein targets by forming C6-2W9G and C1-2W9G with -10.2 and -9.0 kcal/mol, respectively, C6-1N67 and C1-1N67 complexes with -9.9 and -9.8 kcal/mol, respectively, and C1-1MWT and C6-1MWT with -8.8 and -8.0 kcal/mol, respectively (Table 5). Nguyen *et al.*, also used the same target proteins, 2W9G and 1N67, to evaluate the anti-*Staphylococcus aureus* activity of several substances (Nguyen *et al*., 2024) [38]. The free binding energies obtained from this study are slightly higher (ranging from -10.0 to -10.4 kcal/mol) than the free binding energies of C6-2W9G and C6-1N67.

The compound C5 gave good results, although slightly less interesting in terms of free binding energy compared to naringin (C6). The complexes C5-2W9G, C5-1N67, and C5-1MWT were formed with free binding energies of -8.3, -7.9, and -6.3 kcal/mol, respectively. Subsequently, quinic acid (C4) gave the weakest free interaction energies of -6.8, -6.7, and -5.5 kcal/mol for the complexes C4-2W9G, C4-1N67, and C4-1MWT, respectively.

In 2022, a study was conducted by Nanjundaswamy *et al.* on the synthesis and antibacterial evaluation of 3-(pyridin-4-yl)-1-(thiophen-2-yl) (Comp 1) and 3-mesityl-1-(thiophen-2-yl)prop-2-en-1-one (Comp 2) through *in silico* methods using the target protein 1MWT. The free binding energies of Comp 1-1MWT and Comp 2-1MWT were -6.0 and -6.9 kcal/mol, respectively (Nanjundaswamy *et al*., 2022) [36]. These results are less significant compared to those obtained from compounds derived from the flower extract (C1 and C6) of *Rhizophora mucronata*.

Table 5 The three best free binding energies for the complex formed **CX-protein** (X= 1, 4, 5, and 6).

Compounds	Protein ID								
	2W9G			1N67			1MWT chain B		
C1	-9.0	-8.7	-8.0	-9.8	-9.7	-9.6	-8.8	-7.6	-7.4
C4	-6.8	-5.8	-5.7	-6.7	-6.4	-6.2	-5.5	-5.3	-5.2
C5	-8.3	-7.8	-7.7	-7.9	-7.8	-7.7	-6.3	-6.1	-6.0
C6	-10.2	-9.2	-9.1	-9.9	-9.6	-9.6	-8.0	-7.6	-7.5

Attention will be directed towards the interactions underlying the formation of the naringin-protein complex, given its high affinity for the three target proteins (Table 5).

Among the four compounds present in the flower extract, naringin exhibited the best in silico binding affinity, apart from the 1MWT protein, where the C6-1MWT complex showed a free binding energy of -8.0 kcal/mol, compared to -8.8 kcal/mol for C1-1MWT. The C6-2W9G and C6-1N67 complexes demonstrated binding free energies of -10.2 and -9.9 kcal/mol, respectively. Naringin displayed a stronger affinity for the 2W9G protein than the other compounds. The C6-2W9G complex was stabilized by four types of

intermolecular interactions: (i) three conventional hydrogen bonds between the ether group (-O-) and the amino acid THR46 of the protein (with a bond distance of 2.36 Å), as well as two additional hydrogen bonds between the hydroxyl groups of C6 and the amino acid ASN18, with bond distances of 2.89 Å and 2.60 Å; (ii) five carbon-hydrogen bonds between the hydroxyl groups, the *o*-heterocyclic group, and the ether function of the C6 compound and the amino acids SER49, GLY93, GLY94, and PHE92 of the 2W9G protein, with bond distances ranging from 3.53 to 3.72 Å; (iii) a 3.87 Å pi-sigma interaction between the phenolic group and the amino acid LEU28; and (iv) two pi-alkyl interactions between two phenolic groups and the amino acids LEU20 and ILE50, with distances of 4.40 and 4.32 Å, respectively (Table S4, Supporting Information). In comparison, the free binding energies of C6-1N67 and C1-1N67 are very nearby, differing by only ± 0.1 kcal/mol (Table 5 and Figure 7).

The intermolecular interactions of the C6-1N67 complex are as follows: (i) Conventional hydrogen bonds, forming four interactions between the hydroxyl groups of naringin (C6) and the amino acids ARG395, ASN284, and ILE339, with distances ranging from 1.92 to 2.80 Å; (ii) T-shaped pi-pi interactions, involving a bond between a phenolic group and the amino acid PHE449, with a distance of 5.16 Å; (iii) Alkyl interactions between the methyl group of naringin (C6) and the amino acids PRO251, VAL288, and PRO341, with bond lengths of 5.37, 4.27, and 5.11 Å, respectively; (iv) Finally, pi-alkyl interactions, forming two bonds between two phenolic groups of C6 and the amino acids PRO341 and PRO452, with distances of 5.22 and 4.05 Å, respectively (Figure7).

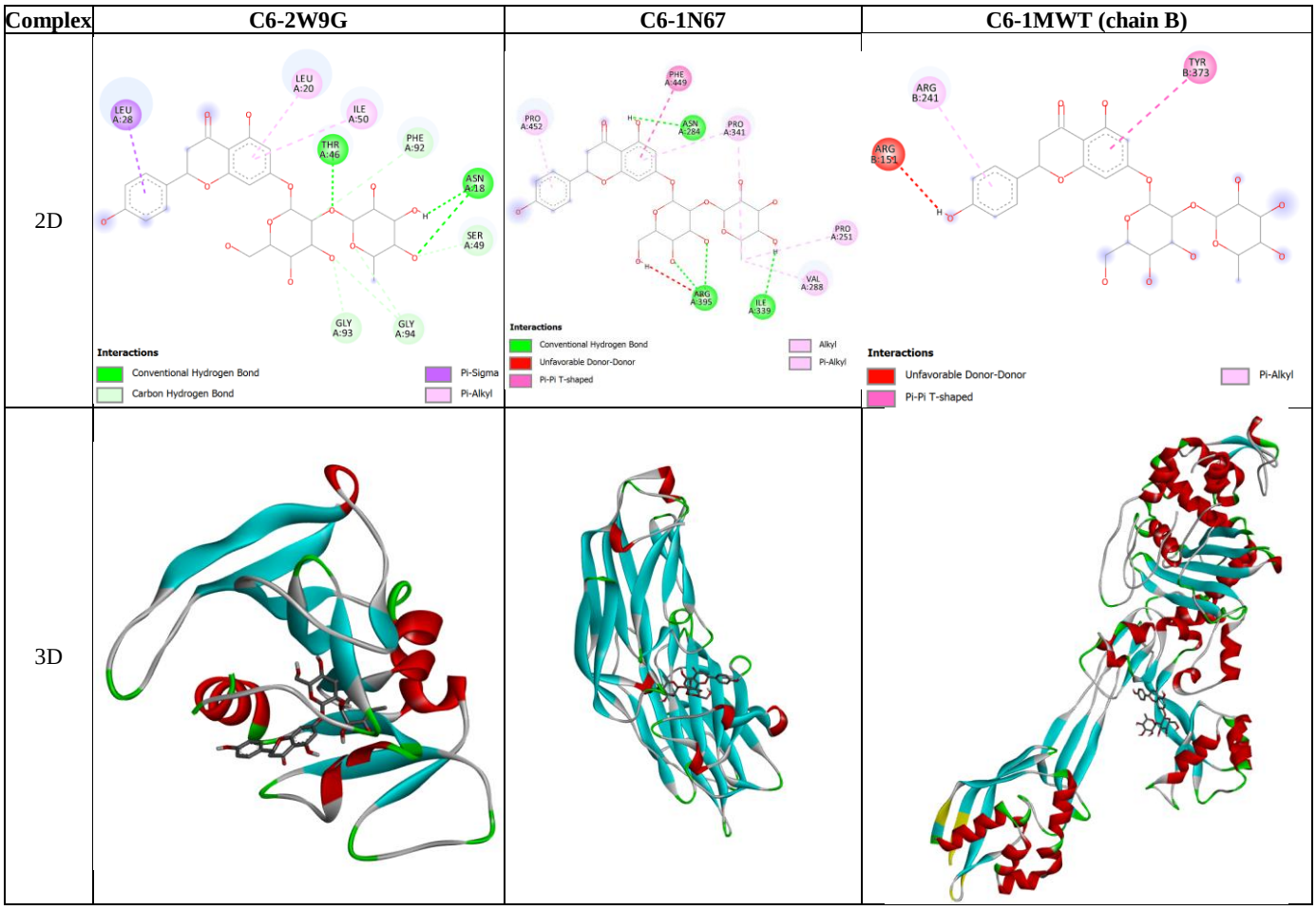

Fig 7: 2D and 3D best three docking interactions between naringin (C6) and three proteins (PDB: 2W9G, 1N67, and 1MWT).

Rutin (C1) also shows the best interaction with protein 1N67 (-9.8 kcal/mol) compared to 2W9G and 1MWT. These interactions are characterized by the presence of 11 intermolecular bonds between the amino acids of protein 1N67 and rutin (C1). Four types of bonds are observed: conventional hydrogen bonds between the amino acids TYR399, TYR448, THR397, and ASP240 and the various hydroxyl groups of C1, with distances of 2.39, 2.94, 2.63, and 2.12 Å, respectively; carbon-hydrogen bond between the amino acid VAL288 and the aliphatic -CH_2- chain of rutin (C1) (3.36 Å); alkyl interaction between the methyl group -CH_3 and two amino acids, PRO251 and VAL288, with distances of 5.07 and 4.71 Å, respectively; and finally, π-alkyl interactions, forming two bonds of 5.36 and 4.99 Å between a phenolic group and the amino acids VAL450 and ILE488, respectively, and a bond of 5.27 Å between the methyl group and the amino acid HIS252.

The C1-2W9G complex showed a binding free energy of -9.0 kcal/mol, more interesting than the free binding energy of the C1-1MWT complex with -8.8 kcal/mol. This complex is formed through the following types of interactions: Conventional Hydrogen Bonding, involving seven bonds between the ligand C1 groups and the amino acids GLN19, LEU20, SER49, ASP27, and LEU5; pi-sigma interactions, with two bonds between the cyclic groups of rutin C1 and the amino acids LEU20 and LEU28, at distances of 3.37 and 3.86

Å, respectively; and finally, pi-alkyl interactions, forming two bonds of 4.50 and 4.41 Å between the phenolic groups and the amino acids LEU20 and ILE50, respectively (Figure 8).

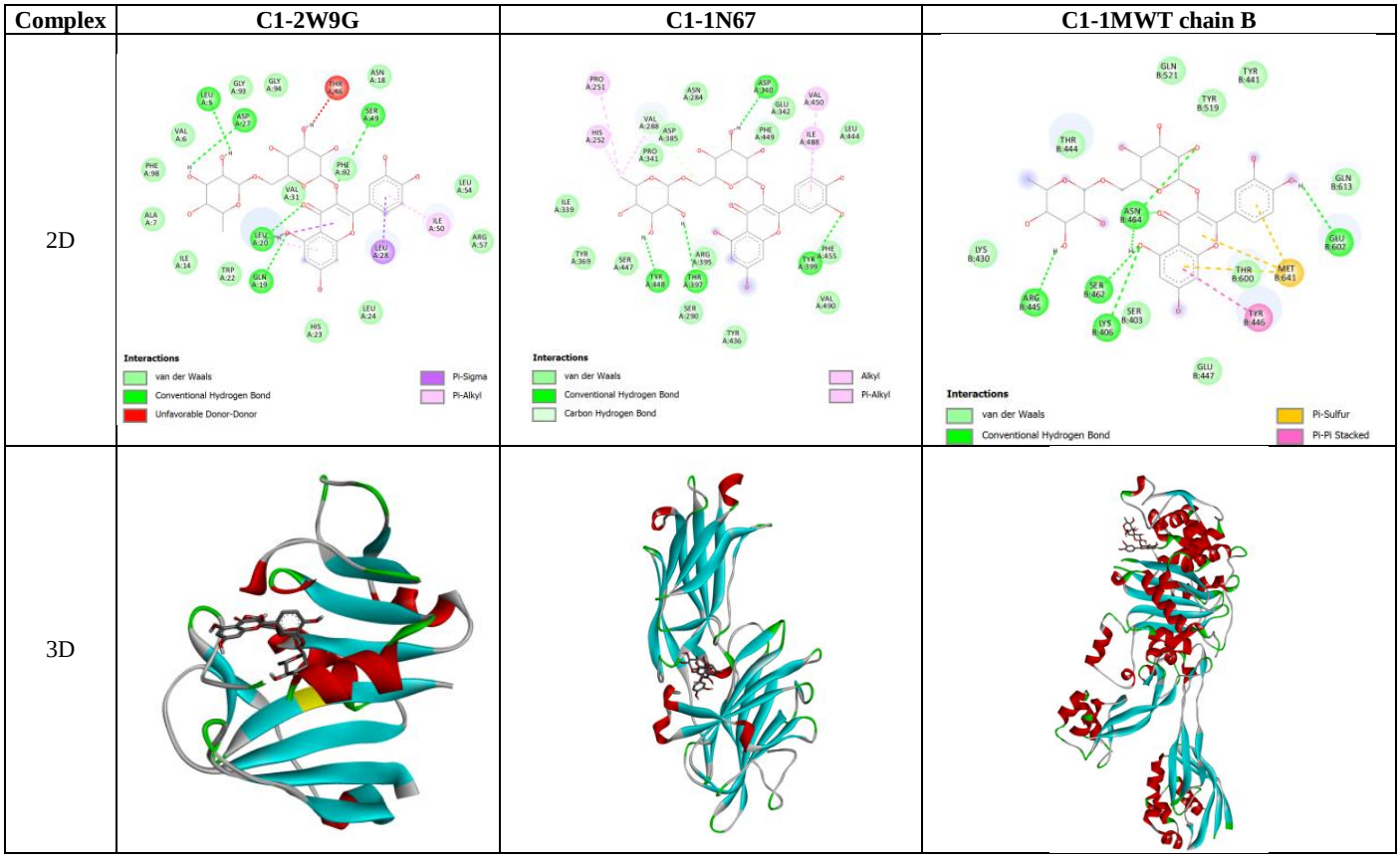

Fig 8: 2D and 3D best three docking interactions between C1 and three proteins (PDB: 2W9G, 1N67, and 1MWT).

Rutin is a flavonoid, a natural compound found in various plants or in certain fruits and vegetables (Cushnie & Lamb, 2005) [9]. It is known for its antioxidant, anti-inflammatory, and vasoprotective properties, but it is not specifically recognized as a direct antibacterial agent against *Staphylococcus aureus* (Morimoto *et al*., 2023) [34]. However, some studies have shown that flavonoids such as rutin may have antimicrobial activity to some extent, including against certain pathogens like *Staphylococcus aureus* (Herlina *et al*., 2024; Miklasińska-Majdanik *et al*., 2023) [17, 32].

It can be concluded that the anti-*Staphylococcus aureus* activity is explained by the cooperativity and synergy of naringin (C6) and rutin (C1) present in the extract of the flower of *Rhizophora mucronata*.

3.5.2. Molecular docking antioxidant screening.

The antioxidant potential of each compound identified by LCMS, present in the ethanolic extracts of *Rhizophora mucronata* was evaluated by *in silico*. The results revealed a good biological response for all the compounds present in the extracts. The different compounds showed interactions with the target protein 2CAG (Table 6). The free interaction energies obtained vary between -11.1 to -5.2 kcal/mol. This work was carried out by choosing 8 conformations to have the best protein-ligand interaction. We limited ourselves to the three best conformations, giving a good protein-ligand affinity. It is observed that the compound C6 gives interesting free binding energy values with -11.1, -10.6, and -10.6 kcal/mol. Compounds C2, C1, and C3 gave close free binding energies compared to compound C6 with values of -9.4, -9.0, and -8.8 kcal/mol for compound C2-2CAG, -9.0, -8.7, and -8.6 kcal/mol for compound C1-2CAG, and -9.0, -8.5, and -8.1 kcal/mol for compound C3-2CAG. Then, compounds C5 andC4 gave less interesting binding energies compared with compounds C6, C2, C1, and C3. The C5-2CAG and C4-2CAG showed weak interactions compared to compound C6-2CAG with energies of -7.1, -6.8, and -6.7 kcal/mol and -6.3, -6.2, and -5.9 kcal/mol, respectively (Table 6).

Table 6: The three best free binding energies for the complex formed CX-2CAG (X= 1 to 6).

Complex	E1 (kcal/mol)	E2 (kcal/mol)	E3 (kcal/mol)
C1-2CAG	-9.0	-8.7	-8.6
C2-2CAG	-9.4	-9.0	-8.8
C3-2CAG	-9.0	-8.5	-8.1
C4-2CAG	-6.3	-6.2	-5.9
C5-2CAG	-7.1	-6.8	-6.7
C6-2CAG	-11.1	-10.6	-10.6

It can be inferred that the C6 compound provided good affinity with the target protein compared to the other compounds C1-5. The free binding energy of the C6-2CAG complex is reflected by a series of interactions between the fragments of the C6 molecule and the amino acids of the 2CAG protein. The C6-2CAG(1) complex is formed by four

types of interactions: Conventional hydrogen bond, pi-cation, pi-pi Stacked, and pi-alkyl. There are approximately two conventional hydrogen bonds: one bond between the *O*-heterocycle group and the amino acids ARG52with distance 2.52 Å; one pi-cation interaction between a phenolic group of the naringin (C6) and the amino acid ARG333 with a distance of 4.85 Å; two bonds pi-pi Stacked interactions: two bonds between two phenolic groups and the amino acids PHE132 and PHE140 with distances of 3.75 and 3.72 Å respectively and finally two bonds pi-alkyl type interactions: two bonds between also phenolic groups and the two amino acids ARG333 and LEU278 with distances of 4.41 and 5.45 Å respectively (Figure 9). The second possibility of interaction to form the C6-2CAG(2) complex is also due to the some type of interaction (carbon hydrogen bond, pi-cation, pi-pi Stacked, and pi-alkyl) but not the same number of interactions. The C6-2CAG(2) complex is formed via a carbon hydrogen bond interaction between the hydroxyl group and the amino acid TYR337 with a distance of 3.54 Å; one pi-cation interactions between phenolic group and the amino acidARG333 (4.81 Å); two pi-pi Stacked interactions between phenolic groups and the amino acidsPHE132 (3.81 Å) and PHE140 (3.70 Å); and two bonds pi-alkyl between also two phenolic groups and the amino acids ARG333 and LEU278 with the distances 4.89 and 5.50 Å respectively. The third proposed C6-2CAG(3) complex is formed by the conventional hydrogen bond, carbon hydrogen bond, pi-cation, pi-pi Stacked, and pi-alkyl interactions as before. Both proposal conformations C6-2CAG(2) and C6-2CAG(3) gave exactly the same free binding energy with -10.6 kcal/mol (Table 7).

Protein2CAG	C6-2CAG (1) (-11.1 kcal/mol)	C6-2CAG (2) (-10.6 kcal/mol)	C6-2CAG (3) (-10.6 kcal/mol)
2D	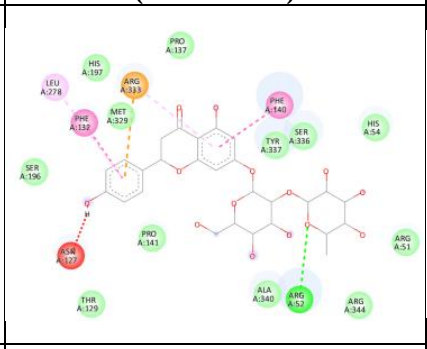	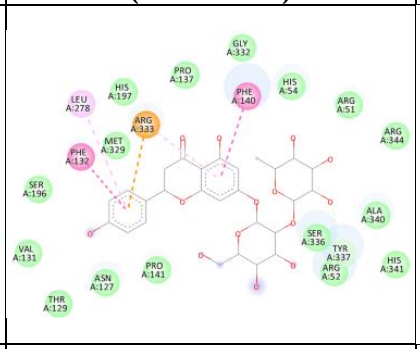	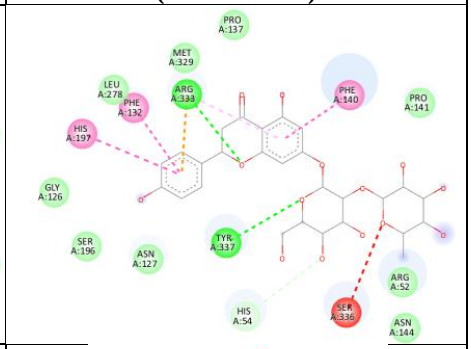
3D	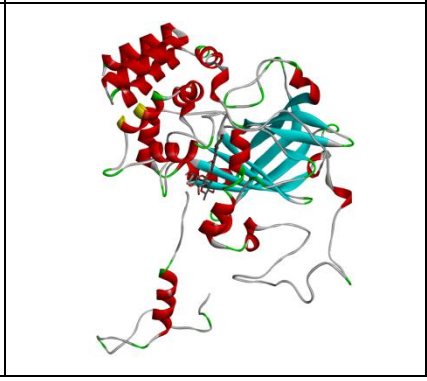	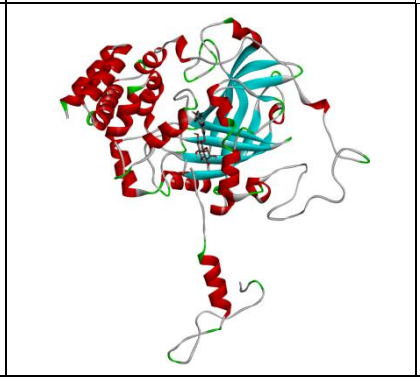	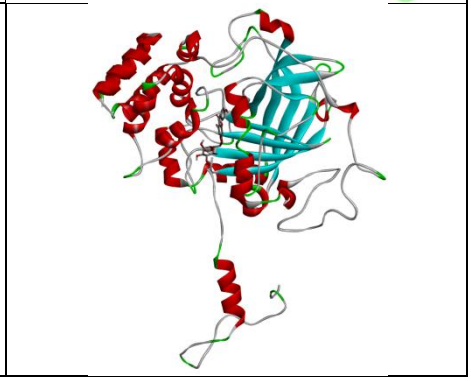

Fig 9: 2D and 3D docking interaction between **C6** and Catalase compound II protein (PDB: 2CAG).

Kaempferol 3-O-α-rhamnopyranoside-7-O-β-glucopyranoside (C2) was exclusively identified in the ethanolic leaf extract and showed a free interaction of C2-2CAG range between -9.4 and -8.1 kcal/mol. The three best interactions for forming the C2-2CAG(1), C2-2CAG(2), and C2-2CAG(3) complexes were -9.4, -9.0, and -8.8 kcal/mol, respectively (Table 6). The C2-2CAG(1) complex is formed by four types of free interactions, specifically four conventional hydrogen bonds between the hydroxyl groups of compound C2 and the amino acids LYS114, ASN355, ASN317, and ASN121, with free bonding energies ranging from -2.16 to -2.82 Å, three carbon-hydrogen bond-type interactions are formed through bridges between a hydroxyl group and two aromatic -CH groups from C2, and the amino acids

Table 7: Best three interaction table between the **C6** compound and Catalase compound II protein (2CAG).

Protein	Compound	Mode	Ligand	Receptor	Interaction type	Interaction category	Distance (Å)	E (kcal/mol)
2CAG	C6	1	O-heterocycle	A:ARG525:HN -NUN:K1:O	Conventional Hydrogen Bond	Hydrogen Bond	2.51889	**-11.1**
			ND	NUN:K1:HN - NUN:K1:O	Hydrogen Bond	Hydrogen Bond	3.74302	
			6 ring phenol	A:ARG333:NH1 - NUN:K1	Pi-Cation	Electrostatic	4.85022	
			6 ring phenol	A:PHE132 - NUN:K1	Pi-Pi Stacked	Hydrophobic	3.79956	
			6 ring phenol	NUN:K1 - A:ARG333	Pi-Alkyl	Hydrophobic	4.78761	
			6 ring phenol	NUN:K1 - A:LEU278	Pi-Alkyl	Hydrophobic	4.18795	
2CAG	C6	2	Hydroxyl - OH	A:TYR327:CA - NUN:K1:O	Carbon Hydrogen Bond	Hydrogen Bond	3.53758	**-10.6**
			O-heterocycle	A:ARG338:NH1 - NUN:K1:O	Conventional Hydrogen Bond	Hydrogen Bond	3.27544	

			6 ring phenol	A:PHE132 - NUN:K1	Pi-Pi Stacked	Hydrophobic	3.87065	
			6 ring phenol	A:PHE118 - NUN:K1	Pi-Pi Stacked	Hydrophobic	3.70295	
			6 ring phenol	NUN:K1 - A:ARG333	Pi-Alkyl	Hydrophobic	4.27651	
2CAG	C6	3	O-heterocycle	A:ARG333:HN - NUN:K1:O	Conventional Hydrogen Bond	Hydrogen Bond	2.53807	**-10.6**
			Hydroxyl - OH	A:HIS543:CD2 - NUN:K1:O	Carbon Hydrogen Bond	Hydrogen Bond	3.54439	
			6 ring phenol	A:ARG333:NH1 - NUN:K1	Pi-Cation	Electrostatic	4.73274	
			6 ring phenol	A:PHE132 - NUN:K1	Pi-Pi Stacked	Hydrophobic	3.79952	
			6 ring phenol	A:HIS191 - NUN:K1	Pi-Pi Stacked	Hydrophobic	3.73121	
			6 ring phenol	NUN:K1 - A:ARG333	Pi-Alkyl	Hydrophobic	4.47765	

HIS350, ASN355, and GLU119, respectively, with distances ranging from 3.40 to 3.60 Å. Additionally, a pi-donor hydrogen bond interaction occurs at 2.73 Å between a **C2** phenol and the amino acid ASN121. Finally, a pi-pi T-shaped interaction is formed between a phenol and the amino acid PHE361 (5.85 Å) (Figure 10).

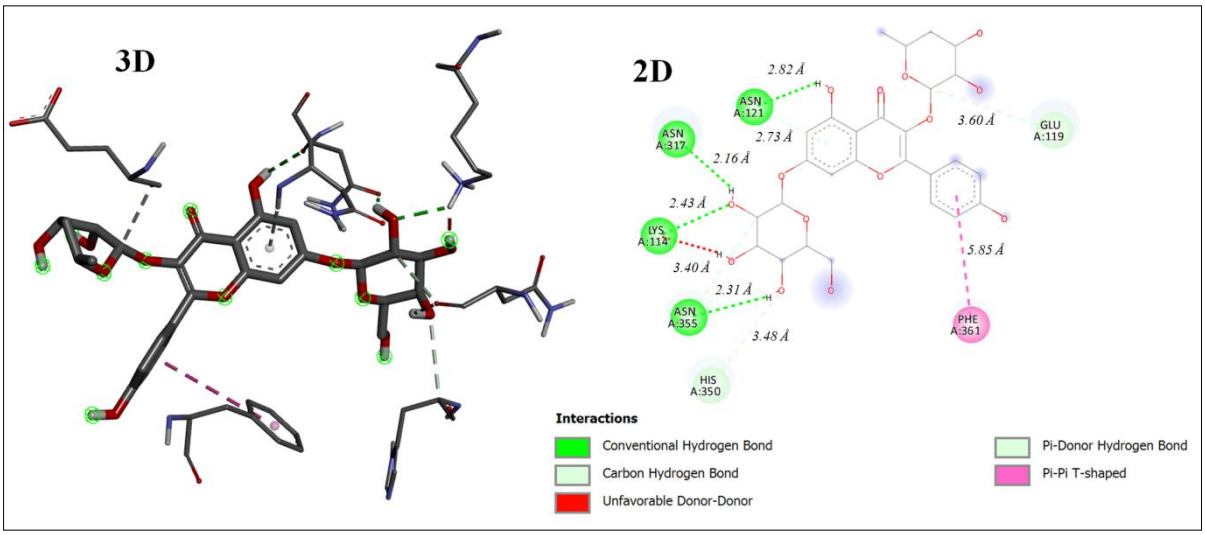

Fig 10: 3D and 2D docking interactions for C2-2CAG(**1)** complex between **C2** and Catalase compound II protein (PDB: 2CAG).

The C2-2CAG(2) complex was also formed by a series of interaction types to give a free binding energy of 9.0 kcal/mol. This energy is explained by conventional hydrogen bond, carbon hydrogen bond, pi-donor hydrogen bond, pi-pi T-shaped and finally pi-alkyl interactions between the compound C2 and the protein 2CAG. The interaction types are the same as the C2-2CAG(1) complex except for the new pi-alkyl interaction between a phenolic group of C2 and the amino acid PRO357 with a distance of 4.64 Å. The C2-2CAG(3) complex is formed with only two interaction types namely conventional hydrogen bond and pi-pi T-shaped in only 4 ponds ligand-protein format between three hydroxyl groups and a phenolic function and the amino acids LYS114, ASN355, HIS365, and PHE361 respectively.

Rutin (C1) and flavone (C3) also gave interesting free binding energy values compared to naringin (C6) and kaempferol 3-O-α-rhamnopyranoside-7-O-β-glucopyranoside (C2) (-11.1*and* 9.4 kcal/mol respectively). The C1-2CAG(1) complex is formed via three types of interactions namely conventional hydrogen bond, pi-pi shaped, and pi-alkyl. A series of six bonds were determined of conventional hydrogen bond type: five interactions between the hydroxyl groups and the amino acids LYS114, ASN355, SER314, and ASN314 with distances ranging from 1.74 to 3.08 Å and one interaction between the *O*-heterocyclic and the amino acid ASN317 with 2.64 Å. We have two pi-pi shaped bonds between the phenolic group and the amino acids PHE361 and HIS365 with distances of 5.03 and 5.26 Å respectively. The pi-alkyl interaction is reflected by the 3.83 Å bond between the methyl group of rutin (C1) and the amino acid ALA316 of the 2CAG protein (Figure 11). The figure also shows an intramolecular interaction *d*(O---O) 2.92 Å between the ketone function and one of the hydroxyl functions. Intramolecular interaction can impact on the intermolecular ligand-protein affinity by occupying two interaction sites. In contrast, the two sites do not participate in any intermolecular bonding with the protein.

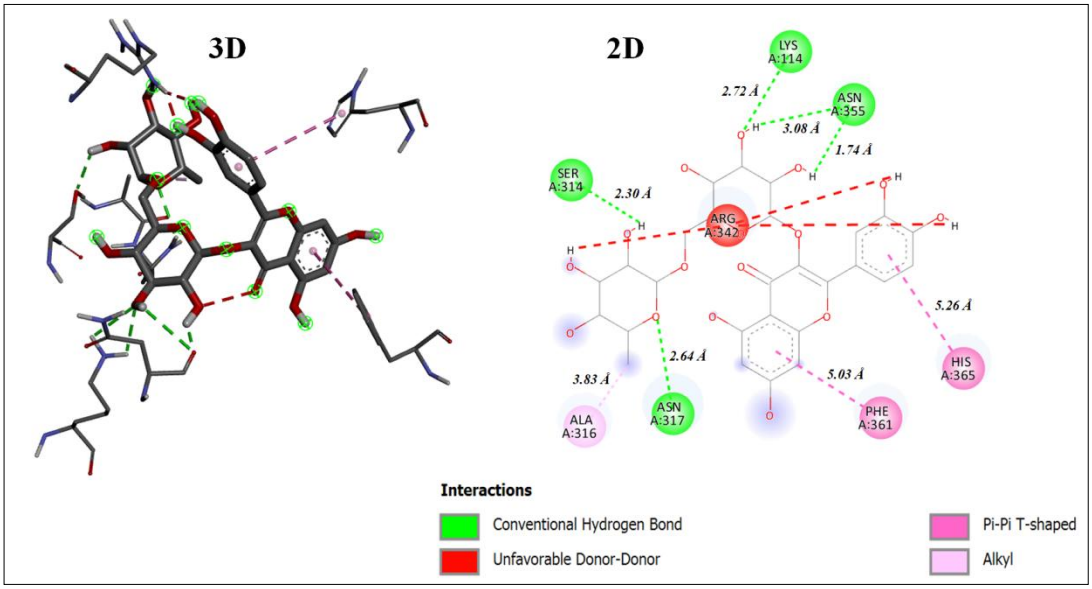

Fig 11: 3D and 2D docking interactions for C1-2CAG(1) complex between Rutin (C1) and Catalase compound II protein (PDB: 2CAG).

The C3-2CAG(1) complex gave the same free binding energy value like C1-2CAG(1) (9.0 kcal/mol). C3-2CAG(1) was formed via a set of four interaction types: conventional hydrogen bond through interactions of the ketone group of the C3 compound and the acids PHE313 and ARG344 with distances of 2.29 and 2.53 Å respectively; carbon hydrogen bond: an interaction of 3.48 Å between the carbon of the ketone function and the acid ALA312; five pi-alkyl type interactions with a distance between 3.93 and 5.14 Å, on the one hand between the phenolic groups and the amino acids ARG51, ALA340, ALA112, and VAL125 and on the other hand between the *o*-heterocylic and the amino acid ARG51 and finally a one pi-pi stacked type interaction between a phenolic group and the amino acid HIS54 with a distance of 4.23Å(Figure12).

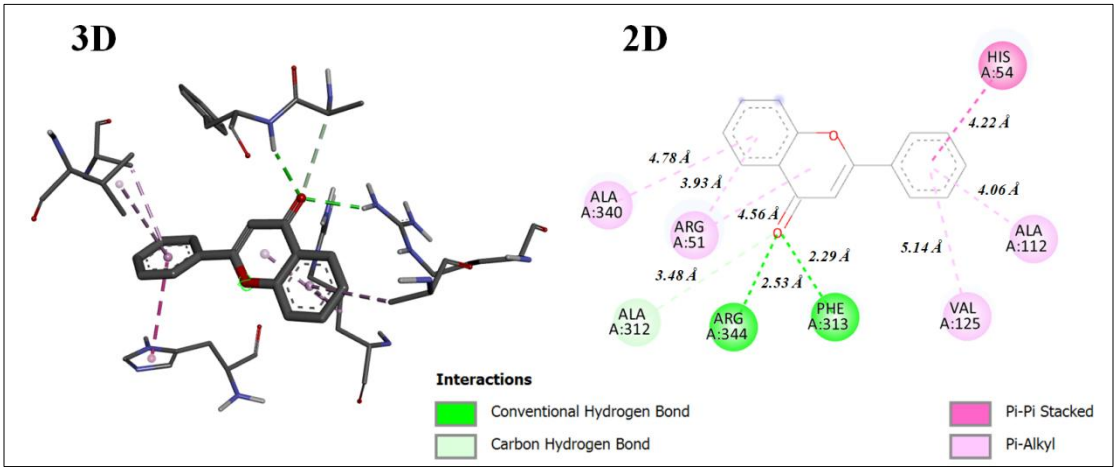

Fig 12: 3D and 2D docking interactions for C3-2CAG(1) complex between flavone (C3) and Catalase compound II protein (PDB: 2CAG).

In terms of free binding energy, it can be concluded that C6 then C2 and C1 compounds respectively showed the best affinities with the 2CAG protein. We can deduce that the flower ethanolic extract is the best extract for antioxidant activity by correlation of the result obtained by LCMS showing the exclusive presence of compound C6.

3.6.3. Molecular dynamics of the best score of antioxidant and antibacterial activities.

3.6.3.1. Molecular Dynamics of C6-2CAG for antioxidant activity.

The Root Mean Square Deviation (RMSD) analysis of the C6-2CAG(1) complex (Figure 13A), provides a detailed characterization of the protein-ligand system's structural stability and dynamic behavior over the 100 ns molecular dynamics simulation. The protein RMSD exhibited a rapid increase during the initial 20 ns, reaching an equilibrium range of 7.5 to 9.0 Å, yet fluctuating without achieving a well-defined stage. This persistent variation suggests ongoing conformational rearrangements, indicating that ligand binding does not rigidly stabilize the protein but instead induces dynamic structural adaptations. Such flexibility may be functionally relevant, enabling the protein to modulate its binding site to accommodate ligand interactions. In contrast, the ligand displayed a more constrained dynamic profile, stabilizing within the 5.5 - 7.0 Å range after initial equilibration. These moderate fluctuations suggest an adaptive binding mode, wherein the ligand remains engaged with the active site while exploring favorable conformations that optimize protein-ligand interactions. The observed stability of the system, despite fluctuations, suggests that the C6-2CAG(1) complex operates within a dynamically flexible binding environment, which may enhance ligand accessibility and reactivity, particularly relevant to its anticipated

antioxidant activity. However, the relatively high RMSD values indicate that C6 binding induces localized structural adaptations, potentially influencing the protein's functional state and interaction landscape.

While the Root Mean Square Fluctuation (RMSF) profile of the C6-2CAG(1) complex (Figure 13B) gives insights into residue-level flexibility, offering a refined perspective on localized structural dynamics throughout the 100 ns simulation. The N-terminal and C-terminal regions exhibited the highest fluctuations, with RMSF values exceeding 9.0 Å, indicative of intrinsically disordered or flexible loop regions. Conversely, the core structured regions remained relatively stable, with fluctuations constrained to ~1.0 - 2.5 Å, indicative of limited conformational variations in the globular domain. Notably, several residues critical to ligand binding exhibited moderate fluctuations, including ARG52, ASN127, PHE132, PHE140, and ASP339, aligning with their role in hydrogen bonding and π-π stacking interactions with naringin (C6). The RMSF values of ~3.0 - 5.0 Å for these residues suggest that, while the ligand remains stably bound, localized conformational adjustments occur within the binding pocket. This is particularly evident for ARG52 and ASP339, previously identified as key stabilizing residues, reinforcing their role in molecular recognition and ligand anchoring. Regions displaying higher flexibility, notably LYS328 - ARG342, suggest adaptive movements that could modulate ligand accommodation and reactivity. The ability of the protein to undergo localized structural adjustments while maintaining overall stability underscores its functional adaptability, a characteristic that may contribute to naringin (C6)'s antioxidant potential by facilitating interactions with reactive species.

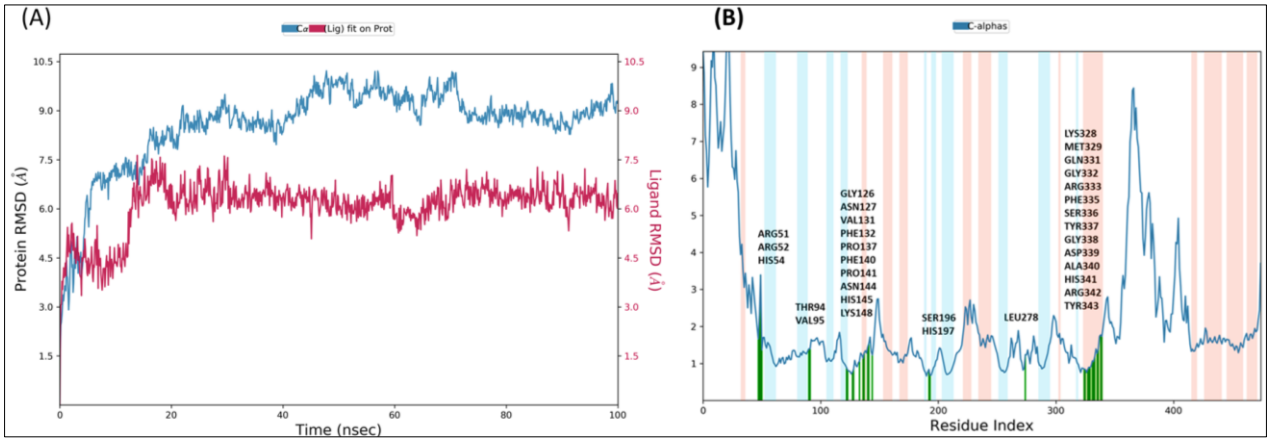

Fig 13: (**A**) Structural stability and (**B**) residue flexibility of the C6-2CAG (1) complex.

Protein-ligand interaction stability and binding mode

The molecular dynamics simulation of the C6-2CAG(1) complex revealed a well-stabilized binding profile, highlighting the ligand's strong affinity for its target protein. ARG52 (57% occupancy) and ASP339 (55% occupancy) were identified as key stabilizing residues, forming persistent hydrogen bonds that were crucial in maintaining complex stability. Additionally, a highly conserved hydrogen bond (98% occupancy) involving a carbonyl group further reinforced the ligand's anchoring within the binding pocket. Beyond hydrogen bonding, π-π stacking interactions with PHE132 (43% occupancy) and PHE140 (47% occupancy) contributed to ligand stabilization, emphasizing the role of hydrophobic contacts in enhancing binding affinity. Time-resolved contact analysis demonstrated that interactions involving ARG52, ASN127, ASN144, PHE132, PHE140, and ASP339 remained stable throughout the 100-ns trajectory, suggesting a well-maintained and persistent binding mode (Figure 14A). The interaction fraction histogram confirmed that hydrogen bonding was the predominant stabilizing force, complemented by hydrophobic and solvent-mediated interactions, which collectively sustained the structural integrity of the complex over time. These findings underscore the strong and enduring binding of C6 to 2CAG, positioning it as a promising antioxidant candidate with a favorable molecular interaction (Figure 14B).

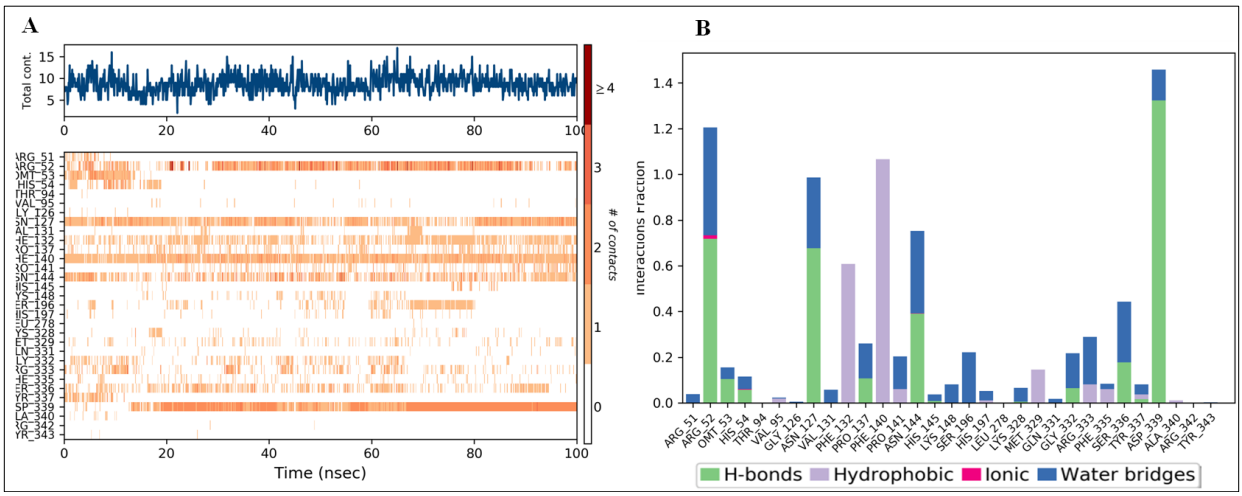

Fig 14: (**A**) Time-resolved contact analysis and (**B**) the interaction fraction histogram for C6-2CAG (1).

3.6.3.2. Molecular Dynamic of C6-2W9G for anti-Staphylococcus aureus.

Building upon the analysis of the C6-2CAG(1) complex, we now proceed to examine the structural dynamics and interaction stability of the second ligand-protein complex under similar conditions. The next section provides a detailed assessment of the RMSD, RMSF, and protein-ligand interaction profiles for the C6-2W9G(1) complex.

The RMSD profile provides insights into the structural stability of the C6-2W9G1 complex over the 100 ns molecular dynamics simulation (Figure 15A). The protein RMSD exhibits an initial increase within the first 40 ns, reaching an equilibrium range of ~1.5 - 2.0 Å, suggesting that the overall protein structure remains well-preserved with only minor conformational adjustments. The absence of significant deviations or large fluctuations indicates a structurally stable protein-ligand system, reinforcing the hypothesis that naringin (C6) binding does not induce substantial destabilization of the receptor. The ligand RMSD, however, demonstrates higher flexibility, with values fluctuating between 5.0 and 7.5 Å, before stabilizing after ~40 ns. These fluctuations suggest that C6 undergoes conformational adjustments within the binding site before reaching a stable binding mode. The eventual convergence of protein and ligand RMSD values indicates that the system achieves a well-equilibrated protein-ligand interaction, highlighting the adaptability of C6M1 in maintaining a stable binding conformation while accommodating structural rearrangements in the active site. The lower protein RMSD compared to C6-2CAG(1) suggests a more rigid and structured binding environment, which may be advantageous for its antibacterial function by ensuring a well-defined interaction mode.

The RMSF profile provides a residue-level assessment of protein flexibility and dynamic adaptation upon ligand binding. As seen in (Fig.3.B), most residues exhibit minimal fluctuations (~0.5 - 2.5 Å), suggesting that the core protein structure remains highly stable throughout the simulation. The relatively low RMSF values observed for key binding residues, highlighted in bold black in the figure, such as SER49, ILE50, THR46, LEU21, and others, indicate that the ligand is anchored within a structurally rigid binding site, further supporting the low protein RMSD values observed in figure 15B. Notably, certain residues exhibit moderate flexibility, particularly ASN18, GLU17, and LEU28, which suggests that localized conformational adjustments occur within the active site. These modest fluctuations (~1.5-2.5 Å) indicate that while C6 remains stably bound, the protein accommodates ligand-induced conformational changes, likely enhancing binding efficiency. The lack of highly flexible loop regions (>3.0 Å) further supports the structural rigidity of the C6-2W9G(1) complex, distinguishing it from the more dynamic C6-2CAG(1) complex.

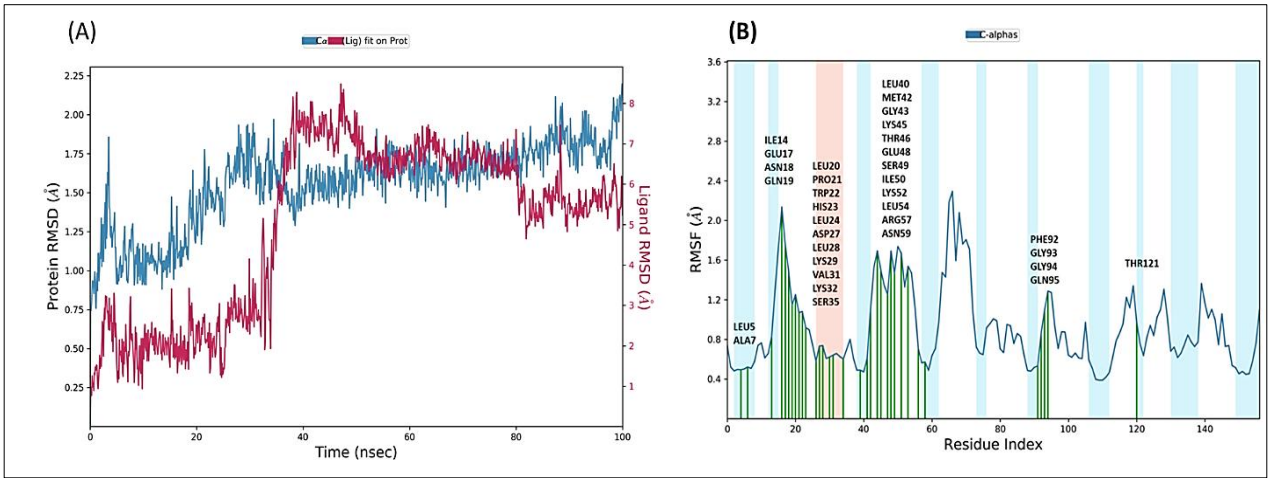

Fig 15: (**A**) RMSD and (**B**) RMSF analysis of the C6-2W9G(1) complex.

The protein-ligand interaction analysis of the C6-2W9G(1) complex provides key insights into the stability and binding mode of the ligand over the 100 ns Molecular Dynamics simulation. The interaction fingerprint (Figure 16) highlights a strong and persistent binding profile, where hydrogen bonding (H-bonds), hydrophobic interactions, ionic interactions, and water bridges collectively stabilize the ligand within the active site. The ligand interaction diagram (Figure 16A) reveals that C6 forms critical hydrogen bonds with SER49 (57% occupancy), SER35 (31% occupancy), and a highly conserved carbonyl group (98% occupancy). These strong H-bond interactions suggest that naringin (C6) maintains a stable profile within the binding pocket, ensuring long-lasting interactions with key residues. Additionally, the time-dependent contact heatmap (Figure 16A) confirms the persistence of interactions with residues such as ASN18, LEU20, THR46, SER49, and ILE50, which remain engaged throughout the trajectory. This indicates that the ligand does not dissociate or lose key contacts, reinforcing the stability of the complex. Furthermore, the interaction fraction histogram (Figure 16B) demonstrates that hydrogen bonds are the predominant stabilizing force, complemented by significant hydrophobic contacts and water-mediated bridges, which enhance ligand affinity. Hydrophobic interactions involving LEU20 and ILE50 contribute to additional stabilization by reducing solvent exposure, while water bridges further reinforce the binding by mediating transient interactions. The presence of ionic and polar interactions suggests that electrostatic contributions also play a role in ligand retention.

These findings indicate that naringin (C6) exhibits a well-defined and persistent binding mode within the 2W9G binding pocket, characterized by strong hydrogen bonding, hydrophobic reinforcement, and dynamic water-mediated interactions. The combination of these stabilizing forces suggests that naringin (C6) maintains a high-affinity interaction, further supporting its potential antibacterial efficacy by ensuring prolonged engagement with the target protein.

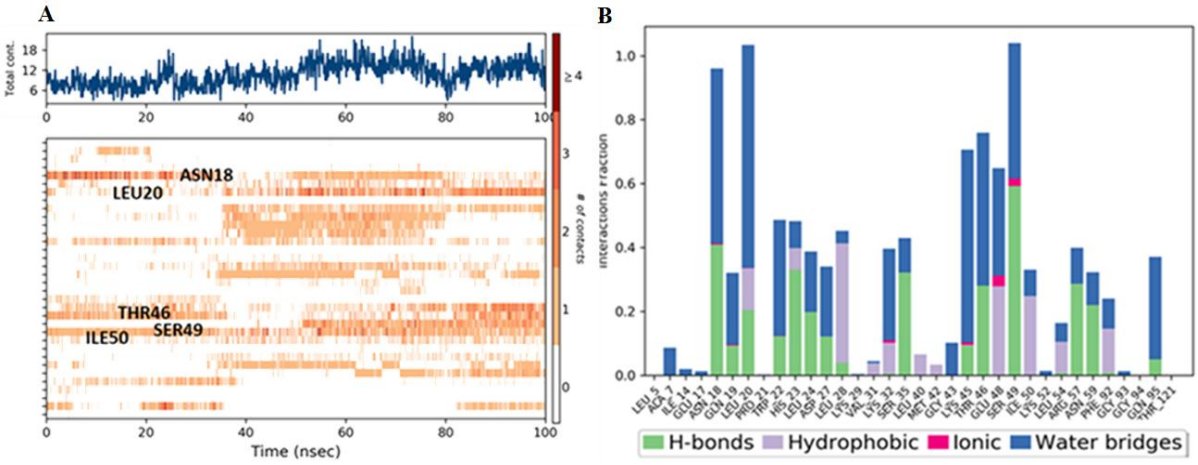

Fig 16: (**A**) Time-resolved contact analysis and (**B**) the interaction fraction histogram for C6-2W9G(1).

These results collectively demonstrate that C6 exhibits distinct interaction dynamics depending on its target protein, with C6-2CAG(1) displaying a more flexible binding environment, allowing for localized conformational adjustments, which may enhance antioxidant activity through dynamic ligand-protein interactions. In contrast, the C6-2W9G(1) complex demonstrated greater structural rigidity, with strong and persistent hydrogen bonding and hydrophobic interactions, suggesting a high-affinity and stable antibacterial binding mode. These findings underscore the differential binding behavior of C6M1, reinforcing its potential multifunctional therapeutic relevance in antioxidant and antibacterial applications.

3.6.4. Toxicity risks assessment.

ADMET (Absorption, Distribution, Metabolism, Excretion, and Toxicity) is an important method in drug design and development processes. The drug-like properties including molecular weight (MW) (< 500), lipophilicity (<5), Hydrogen Bond Acceptor (HBA) (< 10), Hydrogen Bond Donor (HBD) (< 5), Topological Polar Surface Area (TPSA) (<140 Å2), water-solubility (Log S), pharmacokinetics (gastrointestinal absorption, Blood-Brain Barrier, and Permeability) were calculated using Swiss ADME (Manukonda *et al*., 2024) [29] and toxicity (Hepatotoxicity, Neurotoxicity, Respiration toxicity, cardiotoxicity, cytotoxicity, mutagenicity, and LD50) have been performed by using Protox online server (Pokharkar *et al*., 2022) [40].

The molecular weight of compounds C1, C2, and C6 aren't in the range of drug-likeness properties (Mw< 500 g. mol^{-1}) but the compounds C3, C4, and C5 with 222.2, 192.17, and 372.32 g.mol^{-1} respectively, are in the range of drug-likeness properties. All of the compounds discussed in this article adhere to the Lipinski rule of five except the compounds C1, C2, and C6. This means that these compounds C3, C4, and C5 can be used as medicines with only minor modifications to their structure.

As shown in tables 8 and 9, the C3 and C4 compounds showed higher bioavailability (> 0.50) unlike the remain compounds C1, C2, C6 (0.17), and C5 (0.11) to generate main therapeutic agents against antioxidant and/or antibacterial. The solubility of six compounds evaluated ranged from 0.53 to -4.09 mol/L. Compounds C1, C2, and C6 showed suitable water solubility unlike the compound C3 have moderate solubility. The molecules C4 and C5 exhibit excellent solubility with Log S = 0.53 and -1.24 mol/L respectively. It can be deduced that the six compounds showed good to acceptable solubility compared to the references vitamin C (Log S = 0.23 mol/L) and Trolox (Log S = -3.36 mol/L) (Table 8). MLogP is closely related to the drug's lipophilicity, which is a critical component of its solubility, absorption, membrane penetration, plasma protein binding, distribution, and tissue penetration. The drug lipophilicity (MLog P) of the compound varies between 2.27 and -4.05 less than 5, and six compounds are lipophilic (Table 8). According to ADMET characteristics, C1, C2, C4, C5, and C6 have a low rate of human gastrointestinal absorption, whereas only C3have a high rate of human GI absorption and have good rate drug gable properties (Table 9). Furthermore, a detailed examination of the ADMET properties highlights the different attributes that influence the potential of the compounds as antioxidant and/or antibacterial inhibitors. All compounds are generally good candidates; in particular flavone (C3) stands out with an exceptional profile, notably demonstrating robust human intestinal absorption and a balanced combination of desirable properties. This study highlights the crucial role of a comprehensive ADMET profile in the complex drug development process. With its promising attributes, these compounds present a compelling argument for further exploration as potent antioxidant and antibacterial inhibitors.

Table 10 summarizes additional results regarding the toxicological properties of various compounds from the ethanolic extracts of *Rhizophora mucronata*. It can be concluded that the results are acceptable for a potential drug. The median lethal dose (LD_{50}), or median lethal concentration (LC_{50}), is a quantitative indicator of a substance's toxicity. The LD_{50} of compounds C1-6 ranges from 2300 to 9800 $mg{\cdot}kg^{-1}$. It can be inferred that the compounds are slightly toxic (Class 5), except for compound C4, which is very low in toxicity (Class 6) (Table 10).

Table 8: Results of ADME and drug-likeness properties of compounds from ethanolic extracts of *Rhizophora mucronata*.

Compounds	*Mw (g.mol^{-1})*	*MLog P*	*HBA*	*HBD*	*Rot N*	*TPSA (A^2)*	*Solubility*	*Log S (mol/l)*	*Lipinski*	*Veber*	*Bioavailability*
C1	610.52	*-3.89*	*16*	*10*	*6*	269.43	*Soluble*	*-3.30*	*No; 3 violations: MW>500, NorO>10, NHorOH>5*	*No; 1 violation: TPSA>140*	*0.17*
C2	*594.52*	*-3.43*	*15*	*9*	*6*	*249.20*	*Soluble*	*-3.04*	*No; 3 violations: MW>500, NorO>10, NHorOH>5*	*No; 1 violation: TPSA>140*	*0.17*

C3	*222.24*	*2.27*	*2*	*0*	*1*	*30.21*	*Moderately soluble*	*-4.09*	*Yes; 0 violation*	*Yes*	*0.55*
C4	*192.17*	*-2.14*	*6*	*5*	*1*	*118.22*	*Highly soluble*	*0.53*	*Yes; 0 violation*	*Yes*	*0.56*
C5	*372.32*	*-1.89*	*10*	*5*	*8*	*162.98*	*Very soluble*	*-1.24*	*Yes; 0 violation*	*No; 1 violation: TPSA>140*	*0.11*
C6	*580.53*	*-2.77*	*14*	*8*	*6*	*225.06*	*Soluble*	*-2.98*	*No; 3 violations: MW>500, NorO>10, NHorOH>5*	*No; 1 violation: TPSA>140*	*0.17*
Ascorbic acid	*176.12*	*-2.60*	*6*	*4*	*2*	*107.22*	*Highly soluble*	*0.23*	*Yes; 0 violation*	*Yes*	*0.56*
Trolox	*250.29*	*1.81*	*4*	*2*	*1*	*66.76*	*Soluble*	*-3.36*	*Yes; 0 violation*	*Yes*	*0.85*

Table 9: Continuation of table 8.

Compounds	***GI***	***BBB***	***Cyp1A2***	***Cyp2C19***	***Cyp2C9***	***Cyp2D6***	***Cyp3A4***	***Log Kp Skin permeation (cm/s)***	***PAINS Alert***
C1	Low	No	No	No	No	No	No	-10.26	1 alert: catechol_A
C2	Low	No	No	No	No	No	No	-10.35	0 alert
C3	High	Yes	Yes	Yes	No	No	No	-5.13	0 alert
C4	Low	No	No	No	No	No	No	-9.15	0 alert
C5	Low	No	No	No	No	No	No	-9.19	0 alert
C6	Low	No	No	No	No	No	No	-10.15	0 alert
Ascorbic acid	High	No	No	No	No	No	No	-8.54	0 alert
Trolox	High	Yes	No	No	No	No	No	-5.81	0 alert
MW: Molecular Weight, **HBA**: Hydrogen Bond Acceptor, **HBD**: Hydrogen Bond Donor, **TPSA**: Topological Polar Surface Area, **MLogP** = Lipophilicity, **LogS**:Water Solubility, **GI**: Gastrointestinal Absorption, **BBB**: Blood-Brain Barrier.									

Table 10 Toxicological properties of 6 compounds from *Rhizophora mucronata*.

Compounds	**Hepatotoxicity**	**Neurotoxicity**	**Mutagenicity**	**Cytotoxicity**	***Nephrotoxicity***	***Respiration toxicity***	***Cardiotoxicity***	**LD50 ($mg.kg^{-1}$)**	***Classe***
C1	Inactive	Inactive	Inactive	Inactive	Active	Active	Inactive	5000	5
C2	Inactive	Inactive	Inactive	Inactive	Active	Active	Active	5000	5
C3	Inactive	Active	Inactive	Active	Inactive	Inactive	Active	2500	5
C4	Inactive	Inactive	Inactive	Inactive	Active	Inactive	Inactive	9800	6
C5	Inactive	Inactive	Inactive	Inactive	Active	Inactive	Inactive	4000	5
C6	Inactive	Inactive	Inactive	Inactive	Active	Active	Active	2300	5

4. Conclusion

The present study highlights the promising antioxidant and antibacterial potential of bioactive compounds extracted from *Rhizophora mucronata*. Biological activity assays confirmed that ethanolic flower extracts exhibited the most potent antibacterial and antioxidant effects, particularly against *Staphylococcus aureus*. These effects are likely correlated with the presence of naringin and other flavonoids, which were identified as key bioactive agents through molecular docking analyses. Computational simulations provided further insights into the stability and binding affinity of these compounds with bacterial proteins and antioxidant enzymes, reinforcing their potential pharmacological relevance. Molecular dynamics simulations confirmed the stability and adaptability of ligand-protein interactions, particularly for naringin (C6), which exhibited strong binding affinity with key target proteins. The observed structural flexibility suggests a mechanism whereby ligand-induced conformational changes may enhance biological activity, supporting the potential of *Rhizophora mucronata* as a valuable source for pharmaceutical applications. From an applied perspective, the integration of experimental and computational approaches in this study offers a rational framework for drug discovery by combining phytochemical profiling with in silico analysis. The ADMET analysis indicates that some compounds demonstrate favorable bioavailability and toxicity profiles, reinforcing their potential as lead molecules for antioxidant and antibacterial therapeutics. Despite these promising results, some limitations must be acknowledged. While *in vitro* and computational approaches confirm the bioactivity of *Rhizophora mucronata*, further validation through *in vivo* studies and clinical trials is essential to establish its safety and efficacy in real-world applications.

Supplementary Materials: *Figure S1:* Quercetin calibration curve for flavonoid TFC; *Figure S2:* Spectrum and MS/MS of (A) the compound (C1) at 17.94 mn, (B) the compound (C3) at 22.06 mn, and (C) the compound (C2) at 18.63 mn of crude ethanolic leaf extract.; *Figure S3:* Spectrum and MS/MS of (A) the compound (C4) at 1.95 mn, (B) the compound (C5) at 15.49 mn, (C) the compound (C1) at 17.89 mn, and (D) the compound (C6) at 20.35 mn of crude ethanolic flower extract; *Figure S4:* Spectrum and MS/MS of (A) the compound (C4) at 1.94 mn, (B) the compound (C1) at 18.89 mn, and (C) the compound (C3) at 22.04 mn of crude ethanolic stem extract; *Figure S5:* Spectrum and MS/MS of the fragmentation of the compound (C6) at 20.35 mn. ; *Figure S6:* Structural schema of the fragmentation of naringin, as shown in Figure S5. *Table S1:* Measurement of the absorbance of ethanolic extracts at a wavelength of 415 nm characteristic of Quercetin; *Table S2:* Absorbance and RSA of the antioxidant activity result of different crude ethanolic extracts by DPPH method; *Table S3:* Absorbance and RSA of the antioxidant activity result of different crude ethanolic extracts by ABTS method; *Table S4:* Best three interaction table between the C6 compound and protein (2W9G).; *Table S5:* Best three interaction table between the C6 compound and protein

(1N67).; *Table S6:* Best three interaction table between the C6 compound and protein (1MWT).

Acknowledgments: We thank Dr Nabil Mohamed, Minister of Higher Education and Research in Djibouti and Dr Jalludin Mohamed, Director of CERD their constant support. Finaly, the authors greatly acknowledge the Plateforme PhotoNS of the L2CM Laboratory, University of Lorraine.

Reference

1. Adhikari A, Ray M, Das AK, Sur TK. *Antidiabetic* and *antioxidant* activity of *Rhizophora mucronata* leaves (Indian sundarban mangrove): An *in vitro* and *in vivo* study. Ayu. 2016;37(1):76-81. DOI:10.4103/ayu.AYU_182_15
2. Al-Mur BA. Biological activities of *Avicennia marina* roots and leaves regarding their chemical constituents. Arabian Journal for Science and Engineering. 2021;46(6):5407-5419. DOI:10.1007/s13369-020-05272-1
3. Arumugam G, Swamy MK, Sinniah UR. *Plectranthus amboinicus* (Lour.) Spreng: Botanical, *phytochemical*, *pharmacological* and nutritional significance. Molecules. 2016;21(4):369. DOI:10.3390/molecules21040369
4. Bandaranayake WM. Traditional and *medicinal* uses of mangroves. Mangroves and Salt Marshes. 1998;2(3):133-148. DOI:10.1023/A:1009988607044
5. Banerjee P, Eckert AO, Schrey AK, Preissner R. ProTox-II: A webserver for the prediction of *toxicity* of chemicals. Nucleic Acids Research. 2018;46(W1):W257-W263. DOI:10.1093/nar/gky318
6. Camilleri M, Murray JA. *Diarrhea* and *constipation*. In: Loscalzo J, Fauci A, Kasper D, Hauser S, Longo D, Jameson JL, editors. Harrison's Principles of Internal Medicine. 21st ed. New York: McGraw-Hill Education; 2022. p. 1197684491.
7. Chelliah CK, Murugan M, Rajivgandhi G, Gnanasekaran C, Govindan R, Maruthupandy M, Quero F, Arulraj A, Viswanathan MR, Alharbi NS, Alshammary NH. *Phytochemical* derivatives and secondary *metabolites* rich *Rhizophora mucronata* as an active *anti-oxidant* and *anti-bacterial* agent against multi drug resistant bacteria. Journal of King Saud University - Science. 2023;35(8):102912. DOI:10.1016/j.jksus.2023.102912
8. Cruz SM, Marroquín N, Alvarez LE, Chang DE, Cáceres A. Evaluation of mangrove (*Rhizophora mangle* L.) products as coloring, *antimicrobial* and *antioxidant* agents. International Journal of Phytocosmetics and Natural Ingredients. 2015;2(1):1. DOI:10.15171/ijpni.2015.12
9. Cushnie TPT, Lamb AJ. *Antimicrobial* activity of *flavonoids*. International Journal of Antimicrobial Agents. 2005;26(5):343-356. DOI:10.1016/j.ijantimicag.2005.09.002
10. Deivanayagam CCS, Wann ER, Chen W, Carson M, Rajashankar KR, Höök M, Narayana SVL. A novel variant of the *immunoglobulin* fold in surface adhesins of *Staphylococcus aureus*: Crystal structure of the *fibrinogen-binding MSCRAMM*, clumping factor A. The EMBO Journal. 2002;21(24):6660-6672. DOI:10.1093/emboj/cdf619
11. Duke J. Handbook of biologically active *phytochemicals* and their activities. Boca Raton: CRC Press; 1992. p. 1-183.
12. Elmi A, Spina R, Risler A, Philippot S, Mérito A, Duval RE, Abdoul-latif FM, Laurain-Mattar D. Evaluation of *antioxidant* and *antibacterial* activities, *cytotoxicity* of *Acacia seyal* Del bark extracts and isolated compounds. Molecules. 2020;25(10):2392. DOI:10.3390/molecules25102392
13. Falleh H, Ksouri R, Chaieb K, Karray-Bouraoui N, Trabelsi N, Boulaaba M, Abdelly C. *Phenolic* composition of *Cynara cardunculus* L. organs, and their biological activities. Comptes Rendus Biologies. 2008;331(5):372-379. DOI:10.1016/j.crvi.2008.02.008
14. Fareza MS, Choironi NA, Harwoko H, Sunarto S. *Antibacterial* activity of two isolated *endophytic* extracts associated with Indonesian mangrove plant *Rhizophora mucronata*. Pharmaciana. 2018;8(1):169-176. DOI:10.12928/pharmaciana.v8i1.8878
15. Hashem HE, Ahmad S, Kumer A, Bakri YE. *In silico* and *in vitro* prediction of new synthesized N-heterocyclic compounds as *anti-SARS-CoV-2*. Scientific Reports. 2024;14(1):1152. DOI:10.1038/s41598-024-51443-7
16. Heaslet H, Harris M, Fahnoe K, Sarver R, Putz H, Chang J, Subramanyam C, Barreiro G, Miller JR. Structural comparison of chromosomal and exogenous *dihydrofolate reductase* from *Staphylococcus aureus* in complex with the potent inhibitor *trimethoprim*. Proteins: Structure, Function, and Bioinformatics. 2009;76(3):706-717. DOI:10.1002/prot.22383
17. Herlina T, Rizaldi Akili, Abd W, Nishinarizki V, Hardianto A, Latip JB. Review on *antibacterial flavonoids* from genus *Erythrina*: Structure-activity relationship and mode of action. Heliyon. 2024;10:e41395. DOI:10.1016/j.heliyon.2024.e41395
18. Hernández-Rodríguez M, Rosales-Hernández C, Mendieta-Wejebe JE, Martínez-Archundia M, Correa Basurto J. Current tools and methods in *molecular dynamics* (MD) simulations for drug design. Current Medicinal Chemistry. 2016;23(34):3909-3924. DOI:10.2174/0929867323666160530144742
19. Ibrahim HAH, Abdel-Latif HH, Zaghloul EH. *Phytochemical* composition of *Avicennia marina* leaf extract, its *antioxidant*, *antimicrobial* potentials and inhibitory properties on *Pseudomonas fluorescens biofilm*. The Egyptian Journal of Aquatic Research. 2021;47(4):295-301. DOI:10.1016/j.ejar.2021.10.007
20. Ibrahim LF, Elkhateeb A, Marzouk MM, Hussein SR, Abdel-Hameed ESS, Kassem ME. *Flavonoid* investigation, LC-ESIMS profile and *cytotoxic* activity of *Raphanus raphanistrum* L. (*Brassicaceae*). Journal of Chemical and Pharmaceutical Research. 2016;8(7):786-793.
21. Ioakimidis L, Thoukydidis L, Mirza A, Naeem S, Reynisson J. Benchmarking the reliability of QikProp. Correlation between experimental and predicted values. QSAR & Combinatorial Science. 2008;27(4):445-456. DOI:10.1002/qsar.200730051
22. Kaur S, Syed Ali M, Anuradha V, Suganya V, Ashashalini A, Bhuvana P. *In vitro anti-inflammatory* activity of mangrove plant *Rhizophora mucronata* Lam. (*Malpighiales*: *Rhizophoraceae*). Brazilian Journal of Biological Sciences. 2018;5(10):393-402. DOI:10.21472/bjbs.051018
23. Ke Q, Gong X, Liao S, Duan C, Li L. Effects of *thermostats*/*barostats* on physical properties of liquids by *molecular dynamics* simulations. Journal of Molecular Liquids. 2022;365:120116.

DOI:10.1016/j.molliq.2022.120116
24. Kishen A, Sivaperumal P, Roy A, Lakshmi T. *Anticancer* potential from *Rhizophora mucronata* plant leaf associated *Streptomyces* species against the breast cancer cell line. Journal of Pharmaceutical Research International. 2021;33(62B):411-419. DOI:10.9734/jpri/2021/v33i62B35628
25. Krishnamoorthy M, Sasikumar JM, Shamna R, Pandiarajan C, Sofia P, Nagarajan B. *Antioxidant* activities of bark extract from mangroves, *Bruguiera cylindrica* (L.) Blume and *Ceriops decandra* Perr. Indian Journal of Pharmacology. 2011;43(5):557-562. DOI:10.4103/0253-7613.84972
26. Kuppusamy MM, Y NR, N G. Evaluation of *in-vitro antioxidant* and *antibacterial* properties of *Commelina nudiflora* L. extracts prepared by different polar solvents. Saudi Journal of Biological Sciences. 2015;22(3):293-301. DOI:10.1016/j.sjbs.2014.09.016
27. Lim D, Strynadka NCJ. Structural basis for the *β-lactam* resistance of *PBP2a* from *methicillin-resistant Staphylococcus aureus*. Nature Structural Biology. 2002;9(11):870-876. DOI:10.1038/nsb858
28. Mallappa Kumara S, Uma Rani S. *Patchouli* (*Pogostemon cablin* Benth.): Botany, agrotechnology and biotechnological aspects. Industrial Crops and Products. 2016;87:161-176. DOI:10.1016/j.indcrop.2016.04.032
29. Manukonda UK, Ashish S, Anandkumar KP, Akshaykumar HS, Chennu MM PR, Rahit P, Pravin B, Raghavendra NG. Predictive insights into the *ADME* and *toxicological* profiles of *Allium sativum phytochemicals* using *Swiss ADME* and *ProTox-II*. African Journal of Biological Sciences. 2024;6(6):488-509. DOI:10.33472/AFJBS.6.6.2024.488-509
30. Mark P, Nilsson L. Structure and dynamics of the *TIP3P*, *SPC*, and *SPC/E* water models at 298 K. The Journal of Physical Chemistry A. 2001;105(43):9954-9960. DOI:10.1021/jp003020w
31. Mary XA, Mohamed Yacoob SA, Venkatraman A, Packiasamy R, Moovendhan M, Gnanadesigan M, Nagarajan Y. *Anticancer* activity of *Rhizophora mucronata* leaves extract on *Sprague-Dawley* rats: *In vivo* model. Journal of Toxicology. 2023;2023:6665012. DOI:10.1155/2023/6665012
32. Miklasińska-Majdanik M, Kępa M, Wąsik TJ, Zapletal-Pudełko K, Klim M, Wojtyczka RD. The direction of the *antibacterial* effect of *rutin hydrate* and *amikacin*. Antibiotics. 2023;12(9):1469. DOI:10.3390/antibiotics12091469
33. Mohamed AS, Elmi A, Spina R, Kordofani MAY, Laurain-Mattar D, Nour H, Abchir O, Chtita S. *In vitro* and *in silico* analysis for elucidation of *antioxidant* potential of Djiboutian *Avicennia marina* (*Forsk*.) Vierh. *phytochemicals*. Journal of Biomolecular Structure & Dynamics. 2023;42(7):3410-3425. DOI:10.1080/07391102.2023.2213338
34. Morimoto Y, Aiba Y, Miyanaga K, Hishinuma T, Cui L, Baba T, Hiramatsu K. *CID12261165*, a *flavonoid* compound as *antibacterial* agents against *quinolone-resistant Staphylococcus aureus*. Scientific Reports. 2023;13(1):1725. DOI:10.1038/s41598-023-28859-8
35. Nabeelah Bibi S, Fawzi MM, Gokhan Z, Rajesh J, Nadeem N, R R, R K, R Ddg A, Pandian SK. *Ethnopharmacology*, *phytochemistry*, and global distribution of mangroves—A comprehensive review. Marine Drugs. 2019;17(4):231. DOI:10.3390/md17040231
36. Nanjundaswamy S, Gurumallappa, Hema MK, Karthik CS, Rajabathar JR, Arokiyaraj S, Lokanath NK, Mallu P. Synthesis, crystal structure, *in-silico ADMET*, *molecular docking* and *dynamics simulation* studies of *thiophene-chalcone* analogues. Journal of Molecular Structure. 2022;1247:131365. DOI:10.1016/j.molstruc.2021.131365
37. Nejjari R, Raji H, Yamari I, Laghmari M, Touhtouh J, Bakhouch M, Benharref A, Hammani K, Benali T, Mazoir N, Chtita S. Semisynthesis of new *isoxazolines* from (*E*)-*α-atlantone*: *Antibacterial*, *antifungal* activities, *ADME-Tox*, *molecular docking*, and *molecular dynamics* simulations investigations. Journal of Molecular Structure. 2024;1312:138579. DOI:10.1016/j.molstruc.2024.138579
38. Nguyen TTT, Nguyen TTT, Nguyen HD, Nguyen TK, Pham PTV, Tran LTT, Pham HKT, Truong PCH, Tran LT, Tran MH. *Anti-Staphylococcus aureus* potential of compounds from *Ganoderma* sp.: A comprehensive *molecular docking* and *simulation* approaches. Heliyon. 2024;10(7):e28118. DOI:10.1016/j.heliyon.2024.e28118
39. Nur RM, Dewi R, Kaliu S. *Antibacterial* activity of *methanol* extract *Rhizophora mucronata* leaves toward *Salmonella typhi*: Leading the *typhoid* fever. Pharmaciana. 2022;12(3):364-371. DOI:10.12928/pharmaciana.v12i3.22475
40. Pokharkar O, Lakshmanan H, Zyryanov G, Tsurkan M. *In silico* evaluation of *antifungal* compounds from marine sponges against *COVID-19*-associated *mucormycosis*. Marine Drugs. 2022;20(3):215. DOI:10.3390/md20030215
41. Rahmawati, Sanjaya YA, Pratiwi YS, Hendrawan EPN, Salsabila ZN, Amalia T. Potency of mangrove leaves (*Rhizophora mucronata*) containing *bioactive* compounds as source of *antioxidant*: A review. International Journal of Eco-Innovation in Science and Engineering. 2023;4(2):120-128. DOI:10.33005/ijeise.v4i2.120
42. Rohini RM, Das AK. A comparative evaluation of *analgesic* and *anti-inflammatory* activities of *Rhizophora mucronata* bark extracts. Pharmacologyonline. 2009;1:780-791. DOI:10.1080/14786410903315069
43. Roos K, Wu C, Damm W, Reboul M, Stevenson JM, Lu C, Dahlgren MK, Mondal S, Chen W, Wang L, Abel R, Friesner RA, Harder ED. *OPLS3e*: Extending force field coverage for *drug-like* small molecules. Journal of Chemical Theory and Computation. 2019;15(3):1863-1874. DOI:10.1021/acs.jctc.8b01026
44. Rumengan AP, Mandiangan ES, Tanod WA, Paransa DSJ, Paruntu CP, Mantiri DMH. Identification of *pigment* profiles and *antioxidant* activity of *Rhizophora mucronata* mangrove leaves origin Lembeh, North Sulawesi, Indonesia. Biodiversitas Journal of Biological Diversity. 2021;22(7):2963-2970. DOI:10.13057/biodiv/d220730
45. Schwarzbach AE, Ricklefs RE. Systematic affinities of *Rhizophoraceae* and *Anisophylleaceae*, and intergeneric relationships within *Rhizophoraceae*, based on *chloroplast DNA*, *nuclear ribosomal DNA*, and *morphology*. American Journal of Botany. 2000;87(7):547-564. DOI:10.2307/2656599
46. Sur TK, Hazra AK, Bhattacharyya D, Hazra A. *Antiradical* and *antidiabetic* properties of standardized extract of Sunderban mangrove *Rhizophora mucronata*.

Pharmacognosy Magazine. 2015;11(42):389-394. DOI:10.4103/0973-1296.153094
47. Sur TK, Hazra A, Hazra AK, Bhattacharyya D. *Antioxidant* and *hepatoprotective* properties of Indian Sunderban mangrove *Bruguiera gymnorrhiza* L. leave. Journal of Basic and Clinical Pharmacy. 2016;7(3):75-79. DOI:10.4103/0976-0105.183262
48. Toughzaoui A, Chedadi O, El Aissouq A, El Ouardi Y, Bouachrine M, Moradi K, Ouammou A. *Molecular modeling* study for the design of new *TRPV4 antagonists* using *3D-QSAR*, *molecular docking molecular dynamic*, *ADMET* prediction and *retrosynthesis*. Chemistry Africa. 2025;8(1):147-165. DOI:10.1007/s42250-024-01158-z
49. Vittaya L, Charoendat U, Janyong S, Ui-eng J, Leesakul N. Comparative analyses of *saponin*, *phenolic*, and *flavonoid* contents in various parts of *Rhizophora mucronata* and *Rhizophora apiculata* and their growth inhibition of aquatic *pathogenic* bacteria. Journal of Applied Pharmaceutical Science. 2022;12(11):149-158. DOI:10.7324/JAPS.2022.121113
50. Warui MW, Manohar S, Obade P. Current status, utilization, succession and zonation of mangrove ecosystem along Mida Creek, Kenya. International Journal of Bonorowo Wetlands. 2020;10(1):1-11. DOI:10.13057/bonorowo/w100103
51. Xu F, Liu Y, Zhang Z, Yang C, Tian Y. Quasi-MSn identification of *flavanone* 7-*glycoside* isomers in Da Chengqi Tang by *high performance liquid chromatography-tandem mass spectrometry*. Chinese Medicine. 2009;4(1):15. DOI:10.1186/1749-8546-4-15
52. Yousaf MA, Basheera S, Sivanandan S. Inhibition of *Monkeypox* virus *DNA polymerase* using *Moringa oleifera phytochemicals*: *Computational* studies of *drug-likeness*, *molecular docking*, *molecular dynamics simulation* and *density functional theory*. Indian Journal of Microbiology. 2024;64(3):1057-1074. DOI:10.1007/s12088-024-01244-3

Authors Details

Ahmed Said Mohamed
Centre d'Étude et de Recherche de Djibouti, Institut de Recherche Médicinale, Route de l'aéroport, Djibouti

Abdirahman Elmi
Centre d'Étude et de Recherche de Djibouti, Institut de Recherche Médicinale, Route de l'aéroport, Djibouti

Fatouma Mohamed Abdoul-Latif
Centre d'Étude et de Recherche de Djibouti, Institut de Recherche Médicinale, Route de l'aéroport, Djibouti

Rosella Spina
INRAE, LAE, Université de Lorraine, 54000 Nancy, France

Imane Yamari
Laboratory Physical Chemistry of Materials, Faculty of Sciences Ben M'Sik, Hassan II University of Casablanca, B.P. 7955 Sidi Othmane, Casablanca, Morocco

Maha AY Kordofani
Department of Botany, Faculty of Science, University of Khartoum P.O. Box 321, Khartoum, Sudan

Ali Mérito
Centre d'Étude et de Recherche de Djibouti, Institut de Recherche Médicinale, Route de l'aéroport, Djibouti

Arnaud Rislere
Université de Lorraine, CNRS, L2CM, F-54000 Nancy, France

Dominique Laurain-Mattar
INRAE, LAE, Université de Lorraine, 54000 Nancy, France

Samir Chtita
Laboratory Physical Chemistry of Materials, Faculty of Sciences Ben M'Sik, Hassan II University of Casablanca, B.P. 7955 Sidi Othmane, Casablanca, Morocco